PHOTOCHEMISTRY OF AROMATIC HYDROCARBONS: IMPLICATIONS FOR OZONE AND SECONDARY ORGANIC AEROSOL FORMATION

A Dissertation

by

INSEON SUH

Submitted to the Office of Graduate Studies of
Texas A&M University
in partial fulfillment of the requirements for the degree of

DOCTOR OF PHILOSOPHY

May 2005

Major Subject: Atmospheric Sciences

PHOTOCHEMISTRY OF AROMATIC HYDROCARBONS: IMPLICATIONS FOR OZONE AND SECONDARY ORGANIC AEROSOL FORMATION

A Dissertation

by

INSEON SUH

Submitted to Texas A&M University
in partial fulfillment of the requirements
for the degree of

DOCTOR OF PHILOSOPHY

Approved as to style and content by:

Renyi Zhang (Chair of Committee)	Donald R. Collins (Member)
Robert A. Duce (Member)	William H. Marlow (Member)
Richard Orville (Head of Department)	

May 2005

Major Subject: Atmospheric Sciences

ABSTRACT

Photochemistry of Aromatic Hydrocarbons: Implications for Ozone and Secondary Organic Aerosol Formation. (May 2005)

Inseon Suh, B.S., Seoul Women's University;

M.S., Texas A&M University

Chair of Advisory Committee: Dr. Renyi Zhang

Aromatic hydrocarbons constitute an important fraction (~20%) of total volatile organic compounds (VOCs) in the urban atmosphere. A better understanding of the aromatic oxidation and its association in urban and regional ozone and organic aerosol formation is essential to assess the urban air pollution.

This dissertation consists of two parts: (1) theoretical investigation of the toluene oxidation initiated by OH radical using quantum chemical and kinetic calculations to understand the mechanism of O_3 and SOA precursors and (2) experimental investigation of atmospheric new particle formation from aromatic acids. Density functional theory (DFT) and ab initio multiconfigurational calculations have been performed to investigate the OH-toluene reaction. The branching ratios of OH addition to ortho, para, meta, and ipso positions are predicted to be 0.52, 0.34, 0.11, and 0.03, respectively, significantly different from a recent theoretical study of the same reaction system. Aromatic peroxy radicals arising from initial OH and subsequent O_2 additions to the toluene ring are shown to cyclize to form bicyclic radicals rather than undergoing reaction with NO under atmospheric conditions.

Isomerization of bicyclic radicals to more stable epoxide radicals possesses significantly higher barriers and hence has slower rates than O_2 addition to form bicyclic peroxy radicals. At each OH attachment site, only one isomeric pathway via the bicyclic peroxy radical is accessible to lead to ring cleavage. Decomposition of the bicyclic alkoxy radicals leads primarily to formation of glyoxal and methyl glyoxal along with other dicarbonyl compounds.

Atmospheric aerosols often contain a considerable fraction of organic matter, but the role of organic compounds in new nanometer-sized particle formation is highly uncertain. Laboratory experiments show that nucleation of sulfuric acid is considerably enhanced in the presence of aromatic acids. Theoretical calculations identify the formation of an unusually stable aromatic acid-sulfuric acid complex, which likely leads to a reduced nucleation barrier. The results imply that the interaction between organic and sulfuric acids promotes efficient formation of organic and sulfate aerosols in the polluted atmosphere because of emissions from burning of fossil fuels, which strongly impact human health and global climate.

DEDICATION

To My Parents and My Brother

ACKNOWLEDGEMENTS

First, I would like to thank my advisor, Dr. Renyi Zhang. Throughout my research, his support and direction were consistent and his scientific insights guided me to go the right way and made me overcome lots of problems in the middle of my study. I want to also thank my committee member, Dr. Donald R. Collins, for assistance with the application of the differential mobility analyzer and helpful discussions. I want to also thank my other committee members, Dr. Robert A. Duce and Dr. William H. Marlow, for their helpful comments during this effort.

Certainly, I also appreciate all fellows of the Atmospheric Chemistry Group who have helped me in so many ways throughout this research. Special thanks should be given to Ms. Dan Zhang and Mr. Jun Zhao. For experimental works, they gave me a lot of help. I would also like to thank Mr. Ed Fortner for his help with running ion-drift - chemical ionization mass spectrometry.

Most importantly, not to be forgotten are my parents and my brother for their support from my home country Korea. Their deepest love has been instrumental in my study here in the U.S.A.

The author also acknowledges financial support from, the U.S. Department of Energy's Atmospheric Chemistry Program (DOE-ACP), Robert A. Welch Foundation (A-1417), and Texas Air Research Center (TACR). Acknowledgements also go to the additional funding for the quantum chemical calculations from the Texas A&M

University Supercomputing Facilities and the use of the Laboratory for Molecular Simulations at Texas A&M University.

TABLE OF CONTENTS

Page

CHAPTER Page

LIST OF TABLES

TABLE Page

LIST OF FIGURES

FIGURE Page

FIGURE Page

CHAPTER I

INTRODUCTION

Gas-phase reactions of volatile organic compounds (VOCs) associated with photochemical oxidant cycles are of importance in the formation of tropospheric ozone (O_3) and secondary organic aerosol (SOA). The photochemical oxidation of atmospheric volatile organic compounds (VOCs) leads to ozone, acid, and carbon dioxide formation, with major implications for local and regional air quality, acid deposition, and global climate changes [*IPCC* report,1994; *Seinfeld and Pandis*, 1998]. Emissions of organic compounds also lead to a significant increase in the atmospheric aerosol loading by gas-to-particle conversion [*Kavouras et al*., 1998; *Griffin et al*., 1999; *Blando and Turpin*, 2000], which has direct consequences on human health, visibility, and solar radiation [*Pandis et al*., 1995]. Understanding the role of aerosol particles in climate forcing requires detailed information on the formation of new atmospheric particles and their subsequent growth to larger sizes.

Aromatic hydrocarbons are of great interest in tropospheric chemistry of the urban atmosphere in regards to their abundance and reactivity with respect to ozone and organic aerosol formation. Aromatic hydrocarbons constitute a large fraction (~20%) of the total volatile organic compounds in urban and regional atmospheres [*Nelson et al.,* 1983; *Atkinson et al.*, 1997; *Calvert et al*., 2002]. Emissions of aromatic hydrocarbons are primarily from anthropogenic sources, i.e. emission from automobiles, fuel-based vehicles, and industry [*Sigsby et al.*, 1987; *Seinfeld and Pandis*, 1998]. In addition to

---

This dissertation follows the style and format of the *Journal of Geophysical Research.*

their important role in photochemical ozone production, oxidation of aromatic hydrocarbons leads to formation of non-volatile and semi-volatile organic compounds, which are responsible for secondary organic aerosol (SOA) formation [*Odum et al*., 1997; *Forstner et al*., 1997; *Tobias et al.,* 2001]. Also, the likely formation of toxic epoxide products from aromatic oxidation is of considerable concern [*Yu and Jeffries*, 1997; *Motta el al.,* 2002]. Because the epoxy functional group can serve as an electrophile to attack DNA and nucleosides, epoxides have been considered for their carcinogenicity and mutagenicity properties [*Hemminki*, 1983].

There has been considerable progress in laboratory experiments, field, modeling, and theoretical studies to define the source, distribution, and chemical transformations of aromatic hydrocarbons in the atmosphere, but several key areas still remain uncertain and unexplored. Presently the mechanism responsible for ozone formation from oxidation of aromatic hydrocarbons is poorly understood [*Suh et al*., 2003]. Another major obstacle in understanding the chemistry of aromatic hydrocarbons lies in inadequate information on SOA formation; the formation mechanism of SOA and their chemical compositions remain poorly characterized [*Zhang et al*., 2004].

There has been considerable experimental and theoretical work on the OH-initiated reactions of toluene. Experimental studies have investigated the temperature and pressure dependent rate constant of the initial OH-toluene reaction, and in particular experimental work has been carried out to detect the intermediate radicals from the OH-toluene reactions [*Molina et al*., 1999; *Bohn*, 2001]. Environmental chamber studies have also identified several major products consisting of both ring- retaining and fragmentation compounds [*Odum et al*., 1997; *Forstner et al*., 1997; *Yu and Jeffri*, 1997*; Shepson et al*.,

1984; *Lonneman et al*., 1978; *Smith et al.*, 1998; *Klotz et al*., 1998; *Atkinson et al*., 1994; *Volkamer et al*., 2001]. In previous experimental product studies, the carbon balance is less than 50% [*Atkinson et al.,* 1997; *Seinfeld and Pandis*, 1998]. Even in situations where compounds have been identified as significant reaction products, for instance in the cases of glyoxal and methyl glyoxal, unique routes leading to their formation have not been unambiguously established. Interpretation of the identified reaction products is primarily hindered due to the existence of multiple reaction pathways and steps. Previous theoretical studies have been performed to investigate the structures and energies of the intermediate radicals and products formed from the oxidation of organic compounds. Currently, the detailed mechanism of the various organic species oxidation remains highly speculative.

Several nucleation mechanisms have been proposed to explain new particle formation in the atmosphere. It is commonly recognized that binary nucleation of H_2O-H_2SO_4 is not efficient enough to explain atmospheric new particle formation [*Boy et al.*, 2003]. Progress recently has been made in assessing the importance of ternary water–sulfuric acid–ammonia nucleation [*Weber et al*., 1999; *Ball et al*., 1999], ion-induced nucleation [*Yu and Turco*, 2001; *Lee et al*., 2003], and nucleation involving iodine species [*O'Dowd et al.*, 2002; *Kolb*, 2002]. Homogenous ternary nucleation involving H_2SO_4, H_2O, and NH_3 can occur in the continental boundary layer [*Kulmala et al*, 2000]. The nucleation rate of the ternary system is much higher than that of the binary system. However, this mechanism is not able to explain new particle formation in urban areas due to localized ammonia emission. Ion-induced nucleation can arise in the upper troposphere and lower stratosphere with sufficient sun exposure and low preexisting aerosol surface

area [*Lee et al.*, 2003]. Although this mechanism offers a reasonable explanation for the nucleation event in the upper atmosphere, limits due to the ionization rate are still of concern. Homogeneous nucleation involving iodine species may occur in the marine boundary layer. New particles form from condensable iodine-containing vapors, which are the photolysis products of biogenic iodocarbons emitted from marine algae [*O'Dowd et al.*, 2002]. Presently, it is uncertain which process is dominant in the atmosphere.

The hydrocarbon oxidation initiated by OH, O_3, and NO_3 forms low vapor pressure products that can condense as secondary organic aerosol (SOA) [*Pandis et al.*, 1995]. Experimental studies have identified the chemical species responsible for SOA formation. Major SOA formation has been observed from the oxidation reactions of aromatic hydrocarbons [*Wang et al.*, 1992; *Kleindienst et al*., 1999]. Odum et al. [1997] suggested that the atmospheric aerosol forming potential of whole gasoline can be quantitatively accounted for in terms of the aromatic content of the fuel. The biogenic hydrocarbon oxidation has also been studied for the formation of SOA [*Griffin et al*., 1999]. In addition, several theoretical studies have been performed to investigate the SOA precursors from toluene, xylene, α- and β- pinene, higher alkanes with more than 15 carbon atoms, and C10 to C15 alkenes [*Pandis et al*., 1992]. In addition, adsorption of gaseous species onto particulate mass may affect the chemical composition of organic aerosols. Pankow et al. [1994a] has proposed a gas to particle partition model based on a consideration of equilibrium distribution of a compound between the gas and condensed phases. There has been observed correlation of SOA formation yield with organic aerosol mass concentration by Odum et al. [1997]. According to Leach et al. [1999], both semi-volatile and non-volatile compounds can coexist in the particle phase.

Environmental chamber studies have exclusively identified the precursor organic species for the formation of SOA and estimated the aerosol formation yield of various organic compounds [*Pandis et al*., 1995]. However, the disadvantages of this method are its inability to control the formation of condensable organic species, homogeneous or heterogeneous nucleation of SOAs, and the heterogeneous processes that determine gas to particle partition of organic compounds.

This research focuses on the oxidation mechanism of OH-toluene reactions and its relevance to organic aerosol formation. The dissertation consists two parts: (1) theoretical investigation of the toluene oxidation initiated by OH radical using quantum chemical and kinetic calculations and (2) experimental investigation of new particle formation from aromatic acids. This research provides insight concerning the gas-phase mechanism that leads to formation of ozone and gaseous precursors of organic aerosols and the nucleation process that initiates the formation of SOA. The results hence enhance our understanding of ozone and SOA formation.

CHAPTER II

THEORETICAL STUDY OF TOLUENE REACTION WITH OH*

Density functional theory (DFT) and ab initio molecular orbital calculations have been employed to determine the structures and energies of the isomers of the OH-toluene adduct, the methyl hydroxycyclohexadienyl radical, and their corresponding transition states of formation. Geometry optimizations were performed using density functional theory B3LYP and the single-point energies were computed using second-order Møller-Plesset perturbation theory (MP2) and the coupled-cluster theory with single and double excitations including perturbative corrections for the triple excitations (CCSD(T)). OH addition to toluene is shown to proceed via a van der Waals complex between OH and toluene along the reaction path prior to the transition state. At the B3LYP/6-31G(d,p) level of theory the activation enthalpies of OH addition to toluene range from –1 to –4 kcal mol^{-1}. The zero-point-corrected bonding energies of the OH-toluene adduct radicals are between 16 and 18 kcal mol^{-1}, and OH addition to the ortho addition is energetically most favorable. The rate constants of the formation of the OH-toluene adduct radicals and their corresponding isomeric branching have been calculated using the transition state theory (TST).

2.1 Introduction

Reactions of toluene in the atmosphere are mainly initiated by attack from hydroxyl

* Reprinted from Chemical Physics Letters, 364, Suh, I., D. Zhang, R. Y. Zhang, L. T. Molina, and M. J. Molina, Theoretical Study of OH Addition Reaction to Toluene, 454-462, Copyright 2002, with permission from Elsevier.

radical OH [*Atkinson*, 1994]. The toluene-OH reaction results in minor H-atom abstraction from the methyl group and major OH addition to the aromatic ring. The H-atom abstraction pathway leads to the formation of benzyl radicals. Under tropospheric conditions, the main reaction channel of the benzyl radicals is expected to be O_2 addition. Subsequently, the benzyl peroxy radicals react with NO, leading to the formation of aromatic benzyl aldehyde and benzyl nitrate. The carbonyl group formed can further react with OH, followed by addition of O_2, and the peroxy radical will lead to the formation of carboxylic acid and others to propagate the radical chain reactions. The addition of OH to the aromatic ring results in the formation of the OH-toluene adduct, the methyl hydroxycyclohexadienyl radical, which is accountable for 90% of the OH-toluene reaction. Most products in toluene photooxidation result from subsequent reactions of the methyl hydroxycyclohexadienyl radical, comprising both ring retaining and fragmentation species. Laboratory experiments indicate that the methylhydroxycyclohexadienyl radical reacts rapidly with NO_2 with a room temperature rate constant of 3×10^{-11} cm^3 $molecule^{-1}$ s^{-1} [*Seinfeld and Pandis*, 1998; *Knispel et al.*, 1990]. The reaction of this adduct radical with O_2 has a lower rate constant of 1.8×10^{-16} cm^3 $molecule^{-1}$ s^{-1} at room temperature [*Knispel et al.*, 1990]. Also, rather than reaction with NO, the aromatic peroxy radicals are speculated to cyclize to form bicyclic radicals, which are followed by O_2 addition and subsequent ring fragmentation [*Andino et al.*, 1996]. Hence the organic intermediate radicals play a central role in propagating or terminating the toluene oxidation reactions [*Molina et al.*, 1999]. Especially the initial step of the OH-toluene chain reactions is essential to determine the final production

distributions. Figure 2.1 depicts the possible formation of four OH-toluene adduct isomeric radicals.

Several experimental studies have investigated temperature [*Knispel et al*.,1990; *Perry et al*., 1977] and pressure [*Bourmada et al*., 1988] dependent rate constant of the OH-toluene reaction. The experimental results indicate a negative Arrhenius relation of the rate constant with temperature, corresponding to negative activation energy. Experimental studies of the reaction products of OH-initiated reactions of toluene have also been reported [*Akinson*, 1994; *Sherpson et al*., 1984; *Volkamer et al*., 2001; *Tokmakov and Lin*, 2002]. In the presence of O_2 and NO_x, the identified reaction products include hydroxyl aromatic compounds, 2-, 4-, and 3-NO_2-toluene, glyoxal, methylgloxal, butenedial, etc., which are formed from the ring cleavage. The most abundant hydroxyl aromatic compound has been identified as o-cresol. The analysis of the cresols in the product also allows estimate of the positional selectivity, indicating that OH addition to the ortho position is more preferential [*Smith et al.*, 1998; *Klotz et al*., 1998].

In this Chapter theoretical studies have also been performed to investigate the structures and energetics of the OH-toluene adduct isomers, and comparisons have been made between the present work and previous studies [*Andino et al*., 1996; *Uc et al*., 2000; *Bartolotti et al*., 1995]. The most recent work by Uc et al. [2000] employed both DFT and MP2 methods to obtain equilibrium structures of the OH-toluene adduct isomers, their

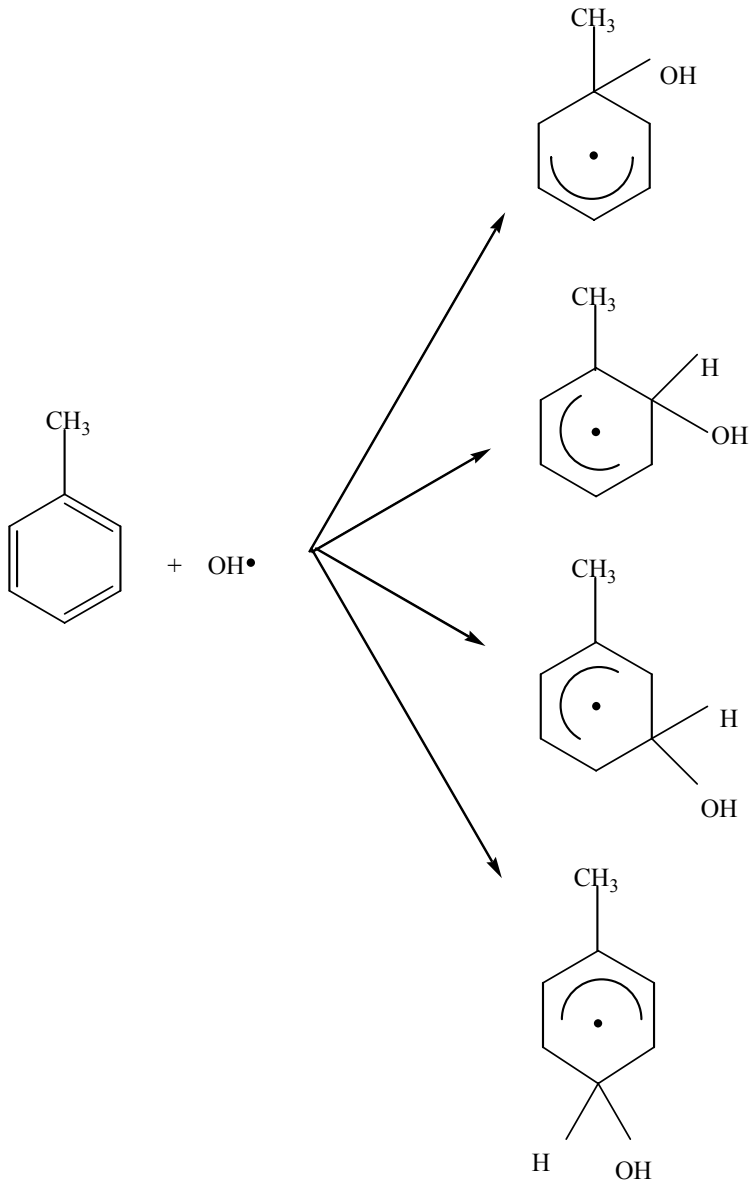

Figure 2.1. A mechanistic diagram for the addition reaction of OH to toluene.

corresponding transition states, and preactivation complexs. The latter authors also evaluated the possible formation of the ipso adduct by OH addition to the methyl substituted site and predicted the statistical occurrence of the OH-toluene isomers on the basis of energetic consideration.

We conduct a theoretical study of the reaction of toluene with OH. Density functional theory (DFT) and ab initio multiconfigurational calculations have been employed to investigate the OH-toluene reaction. The geometries and energetics of the four isomers of the OH-toluene adduct radicals as well as their corresponding transition states are presented. The different DFT and ab initio theories applicable to the OH-toluene reaction system are evaluated. We calculate the rate constant and isomeric branching of the formation of the OH-toluene adduct isomers, using the presently obtained geometries and energetics and the transition state theory (TST).

2.2 Theoretical Methods

The theoretical computations were performed on an SGI Origin 3800 supercomputer using the GAUSSIAN 98 software package[*Frisch et al.,* 1998]. All radicals were treated with the unrestricted Hartree-Fock (UHF) formulation. Geometry optimization was executed using Becke's three parameter hybrid method employing the LYP correction function (B3LYP) in conjunction with the split valence polarized basis set 6-31G(d,p). The DFT structures were then employed in single-point energy calculations using frozen-core second-order Møller-Plesset perturbation theory (MP2) and coupled-cluster theory with single and double excitations including perturbative corrections for the triple excitations (CCSD(T)) with various basis sets. Harmonic

vibrational frequency calculations were made using B3LYP/6-31G(d,p). The geometries of the OH-toluene adducts and their corresponding transition states were also fully optimized at the CASSCF level, to compare the calculated B3LYP and CASSCF geometries. The wavefunction was constructed for configurations made by seven possible occupancies of the active electrons in the subspace of seven active orbitals. In addition, the CASPT2/6-31G(d) method was employed in studying the energetics of the OH-toluene reaction. We corrected basis set effects on the calculated energies for the isomers of the OH-toluene adduct radicals, based on an approach that has been developed and employed to investigate the energetics for several addition reactions related to isoprene [*Lei and Zhang*, 2000; *Suh et al*., 2001]. The procedure involves determination of a correction factor associated with basis set effects at the MP2 level and subsequent correction to the energy calculated at a higher level of electron correlation with a moderate size basis set. For the isomers of the OH-toluene adduct radicals, the basis set effects on the energies were evaluated at the MP2 level. A correction factor, CF, was determined from the energy difference between the MP2/6-31G(d) and MP2/6-311++G (d,p) levels. The values of calculated energies at the CCSD(T)/6-31G(d) level were then corrected by the MP2 level correction factors, corresponding to the CCSD(T)/6-31G(d)+CF level of theory.

Rate constants of unimolecular (k_{uni}) and bimolecular (k_b) reactions of the aromatic intermediate radicals were calculated using classic transition state theory (TST). The high-pressure limit unimolecular rate constant is expressed by [*Lei et al*., 2001; *Zhang et al*., 2003],

$$k_{uni} = \frac{kT}{h}\frac{Q_{AB}^{\ddagger}}{Q_{AB}}\exp\left(-\frac{E_a}{kT}\right) \qquad (2.1)$$

where $Q_{AB}^{\ddagger}$ is the partition function of the transition state with the vibrational frequency corresponding to the reaction coordinate removed, Q_{AB} is the partition function of the reactant, and E_a is the zero-point corrected activation energy. The association rate is related to the dissociation rate by the equilibrium constant (K),

$$\frac{k_{rec}}{k_{uni}} = K = \frac{Q_{AB}}{Q_A Q_B}\exp\left(\frac{D_0}{kT}\right) \qquad (2.2)$$

where Q_{AB} is the partition function of the dissociating species, Q_A and Q_B are the partition functions of the fragmentation products, and D_0 is the zero-point corrected binding energy.

To assess the fate of chemically excited primary peroxy radicals and bicyclic radicals, we evaluated their stabilization and unimolecular isomerization using RRKM/master equation. Briefly, the concentration of a species formed by chemical activation is related to the balance over all gain and loss processes [*Zhang et al*., 2002; *Lei et al*., 2002; *Zhao et al*., 2003],

$$\frac{dn_i}{dt} = Rf_i - \omega n_i + \sum_j P_{ij} n_i - \sum_r k_{ri} n_i \qquad (2.3)$$

where n_i is the concentration of the intermediate having internal energy E_i, R is the overall formation rate, f_i is the normalized energy distribution, P_{ij} is the energy transfer probability from j to i, k_{ri} is the reaction rate constant for the pathway r, and ω is the collision frequency. Exact state counts for vibration density of states were evaluated by using the Beyer-Swinehart algorithm [*Stein and Rabinovitch*, 1973]. The RRKM/ME

calculations employed an exponential model for collision energy transfer using an average energy of 250 cm^{-1} [*Zhang et al*., 2002]. All vibrations were treated as harmonic. We found that explicit treatment of the internal rotors as hindered rotors did not significantly alter the results. Calculations were performed at fixed total angular momentum and subsequently Boltzmann averaged.

2.3 Results and Discussions

2.3.1 OH-Toluene Adduct Radicals

The geometries of the lowest energy conformers for the four isomers of the OH–toluene adduct are illustrated in Figure 2.2 at the B3LYP/6-31G(d,p) level of theory. OH addition results in rearrangements to the aromatic ring. Addition of OH to toluene leads to a lengthening of the C–C bonds adjunct to the site of addition. For the ipso isomer, the C–C bond lengths are increased by 0.11 Å between C1–C2 and C2–C3 and by 0.03 Å between C1 and the methyl carbon (C7). The increased C–C bond length adjacent to the OH addition site reflects an increased r character, as electron density is transferred to the newly formed C–O bonds. On the other hand, the C–C bond lengths are shortened by about 0.02 Å between C2–C3 and C5–C6, but are lengthened by about 0.02 Å between C3–C4 and C4–C5. These bond lengths are between the typical values for a σ bond and π bond. An examination of the total atomic spin density reveals the values of about 0.4 and 0.6 for the carbons adjacent to and opposite to the addition site, respectively, indicating the formation of delocalized double bonds in a resonance structure involving carbons 2–6.

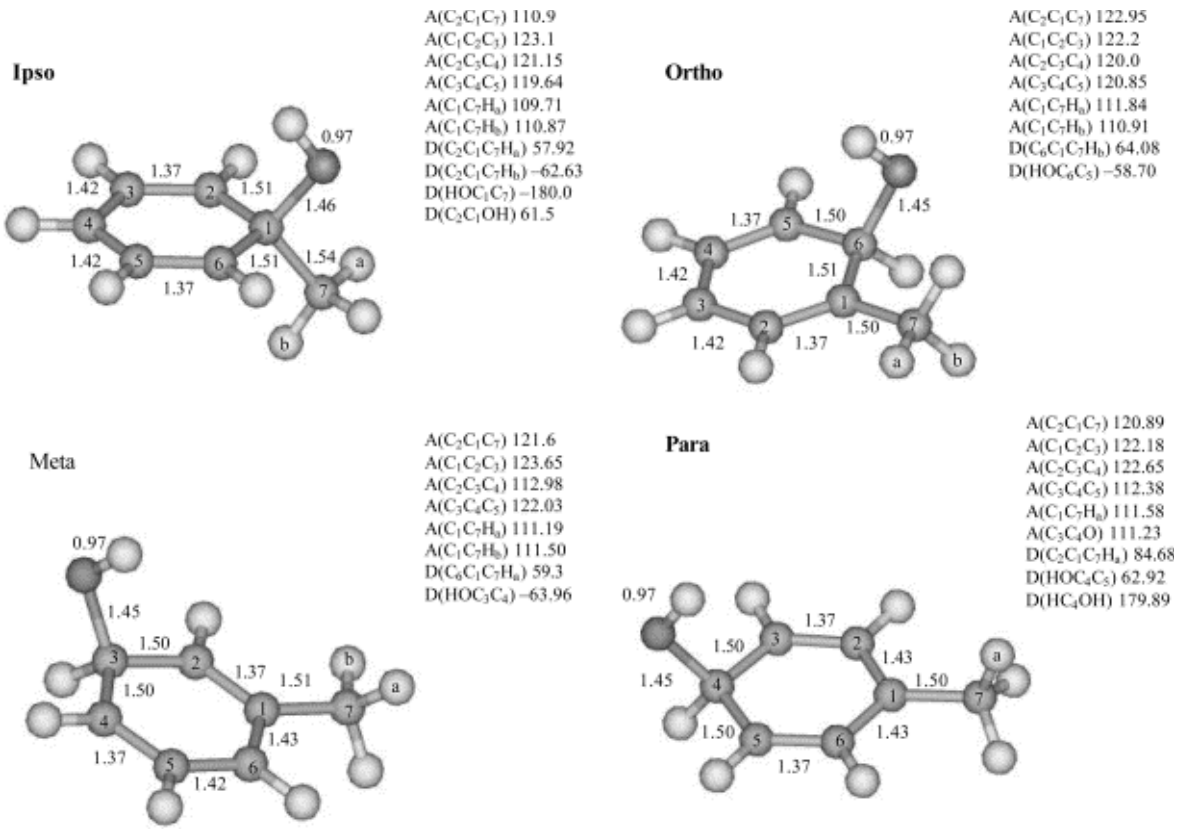

Figure 2.2. Optimized geometries of the four isomers of the methyl hydroxycyclohexadienyl radicals calculated at the B3LYP/6-31G(d,p) level of theory (bond lengths in angstroms and angles in degrees).

(The values of unity and zero for the total atomic spin density correspond to one and zero unpaired electron, respectively.) Similar C–C bonding characteristics are observed for OH addition at the ortho, para, and meta positions. The C–O bond distance in all four isomers is between 1.45 and 1.46 Å. Also, the aromatic ring is symmetric for ipso and para additions, but is slightly non-symmetric for ortho and meta additions. The CASSCF geometries are similar to those obtained using B3LYP/6-31G(d,p).

Spin contamination with the B3LYP optimized geometries of the four adduct radical isomers is minimal. The calculated spin eigenvalues, <S**2>, are between 0.786 and 0.789 for the four adduct isomers. After the S + 1 component is annihilated, the values of <S**2> are reduced to 0.751 for all four isomers, which is nearly identical to the exact value of a pure doublet. This implies that contamination of the unrestricted Hartree–Fock wavefunction from higher spin states is negligible for the four adduct radicals. However, the spin eigenvalues related to the CCSD(T) single-point energy calculations are about 1.19 before spin projection, and are reduced to about 0.975 after spin projection, indicating significant spin contamination. Similarly, we also found significant spin contamination in the MP2 single-point energy calculations.

Results of the calculated reaction (binding) energies of the four isomers of the OH–toluene adduct are listed in Table 2.1. Table 2.1 reveals that the calculated reaction energies are sensitive to both electron correlation and basis set effects. The binding energies obtained by using B3LYP/ 6-31G(d,p) range from 16.0 to 17.6 kcal mol^{-1}. The binding energies predicted by CCSD(T)/6-31G(d) are smaller than those calculated using B3LYP/6-31G(d,p), by 2–4 kcal mol^{-1}. Inclusion of the basis set correction factor to the CCSD(T) method reduces the difference in the reaction energies between B3LYP/6-

31G(d,p) and CCSD(T)/6-31G(d)+CF. Also, the MP2 method produces rather unreliable reaction energies, since OH addition to the meta or para position is predicted to be endothermic. The largest binding energies for the OH–toluene adducts were predicted at the CASPT2/6-31G(d) level of theory, ranging from 21.2 to 25 kcal mol^{-1}. A previous experimental study reported the reaction energies for the OH–toluene reaction on the basis of the measured rate constants as a function of temperature [*Perry et al*., 1977]. The experimental value of the reaction energy is □16.5 ± 5 kcal mol^{-1}. Hence the DFT method produces the binding energies in better agreement with the experimental value than the other methods. A recent theoretical study by Uc et al. [2000] also determined the reaction energies in the range of □19.4 to □21.0 kcal mol^{-1} using B3LYP/6-31G(d,p), which are about 3.2–3.3 kcal mol^{-1} higher than our values. Since the comparison is made by employing the same level of theory in the energy calculations, a difference in the reaction energy of such magnitude is not anticipated. The origin of this disparity is unclear. Also included in Table 2.2 is the standard enthalpies of formation for the lowest energy isomers, estimated from the calculated total energy (*E*), the experimentally known enthalpies of formation for the reactants, and thermal energy (*TE*) correction obtained from the frequency calculations.

Table 2.1. Zero-point corrected reaction energies, *RE*(kcal mol^{-1}), and enthalpies of formation, ΔH_f (kcal mol^{-1}), for the toluene–OH adduct isomers.

	B3LYP /6-31g(d,p)	CCSD(T)/6-31G(d)	CCSD(T)/6-31G(d) + CF	CASPT2/6-31g(d)	ΔH^0_f (B3LYP/6-31G(d,p))
ipso	-16.33	-14.24	-15.54	-24.95	3.77
ortho	-17.56	-13.73	-14.09	-24.06	2.63
meta	-16.04	-12.28	-13.02	-21.28	4.22
para	-16.71	-12.73	-13.33	-22.05	3.68

Table 2.2. Zero-point corrected activation energies (kcal mol^{-1}) for OH addition reactions to toluene.

	B3LYP/6-31g(d,p)[a]	B3LYP/6-311G (2df,2p)[b]	B3LYP/6-311G (3df,2p)[a]	CCSD(T)/6-31G(d)[a]	CCSD(T)/6-31G(d) + CF[a]	CASPT2/6-31g(d)[c]
ipso	-1.65	-1.70	-2.15	4.69	3.27	10.74
ortho	-3.17	-3.23	-3.58	4.11	3.14	10.15
meta	-1.54	-1.39	-1.87	5.78	4.92	11.82
para	-2.08	-1.97	-2.49	5.41	4.55	11.71

[a] Using B3LYP/6-31G(d,p) optimized geometry.
[b] Using B3LYP/6-311G(2df,2p) optimized geometry.
[c] Using CASSCF/6-31G(d) optimized geometry.

The single-point energies of all the reactants and products and the thermal energy (*TE*) correction were based on calculations at the B3LYP/6-31G(d,p)//B3LYP/6-31G(d,p) level of theory. The enthalpy of reaction (ΔE) for the addition reaction of OH to toluene is expressed by

$$\Delta E = [E(\text{Adduct}) - E(\text{Toluene}) - E(\text{OH})] + [TE(\text{Adduct}) - TE(\text{Toluene}) - TE(\text{OH})] \quad (2.4)$$

Alternatively, the enthalpy of reaction between OH and toluene is given as

$$\Delta E = \Delta H_f^o(\text{Adduct}) - \Delta H_f^o(\text{Toluene}) - \Delta H_f^o(\text{OH}) \quad (2.5)$$

where ΔH_f^o(Toluene) and ΔH_f^o(OH) are the enthalpies of formation for toluene and OH, with values of 12.1 and 9.3 kcal mol^{-1}. The enthalpies of formation for the four OH–toluene adduct isomers are 3.8, 2.6, 4.2, and 3.7 kcal mol^{-1} for the ipso, ortho, meta, and para isomers, respectively. The previous experimental work by Perry et al. [1977] determined a value of 0.8 ± 3.0 kcal mol^{-1} for the enthalpy of formation of the OH–toluene adduct. The experimental value is somewhat different from this study, but the difference is close to the quoted experimental uncertainty.

2.3.2 Transition States for the Formation of OH-Toluene Adduct Isomers

Figure 2.3 illustrates the transition state structures of the OH–toluene reaction. The C–O distances of the transition states are between 2.03 and 2.06 Å, 0.58–0.61 Å longer than those of the corresponding OH–toluene adduct isomers. A comparison between the structures of toluene, the adduct isomers, and the transition states clearly reveals the intermediate features in the transition state structures. We also examined the effect of expansion of polarization function on the equilibrium geometries of the

transition states. Additional geometry optimization of the four transition states was carried out using B3LYP/6-311G(2df,2p), and the optimized structures are very similar between the two basis sets of 6-31G(d,p) and 6-311G(2df,2p). In addition, the CASSCF geometries for the transition states are similar to the corresponding B3LYP geometries.

As is the case with the OH–toluene adduct isomers, spin contamination for the transition states is minimal using B3LYP. The values of <S**2> are in the range 0.77–0.79 before projection, and are reduced to about 0.75 after projections. On the other hand, the spin contamination is significant using MP2 and CCSD(T) for single-point energy calculations. The spin eigenvalues associated with the CCSD(T) method are in the ranges 1.40–1.42 before and 1.06–1.14 after spin projection.

The activation energies for the OH–toluene adduct formation are provided in Table 2.2. The B3LYP/6-31G(d,p) method predicts negative activation energies for all four OH addition pathways, with the lowest and highest values of –3.23 and –1.39 kcal mol^{-1} corresponding to TS_o and TS_m, respectively. The activation energies obtained with B3LYP/6-311G(2df,2p) for geometry optimization are very similar to those determined with B3LYP/6-31G(d,p). Both the MP2 and CCSD(T) methods produce positive activation energies. The activation energies calculated with MP2 are too high to be realistic. The activation energies determined with CCSD(T) are in the range 4.11–5.78 kcal mol^{-1}. We also employed the basis set correction method discussed above to determine the activation energies of the OH–toluene reaction, by correcting the CCSD(T)/6-31G(d) energies with the correction factors developed at the MP2 level of theory. This method slightly reduces the activation energies. The activation energies obtained at the CCSD(T)/6-31G(d)+CF level of theory are 3.13 kcal mol^{-1} for the ortho

adduct and 3.2 kcal mol^{-1} for the ipso adduct. As is discussed above, both the MP2 and CCSD(T) methods suffer considerably from spin contamination in the calculations of the energetics of the OH–toluene adduct isomers and their corresponding transition states, and hence the activation energies obtained with the two methods are unreliable. The CASPT2/6-31G(d) method also predicts much higher activation energies than B3LYP/6-31G(d,p), with the values of 10–12 kcal mol^{-1}. On the other hand, the methods using B3LYP/6-31G(d), CASPT2/6-31G(d), and CCSD(T)/6-31G(d)+CF consistently predict the smallest activation energy for the ortho pathway. Figure 4.4 depicts the potential energy surface for the formation of the OH–toluene adducts at theB3LYP/6-31G(d,p) level of theory. Based on the measurements of the temperature-dependent rate constant, the activation energy of the OH–toluene reaction has been previously inferred, with a value of □1.6 ± 1.0 kcal mol^{-1} in the temperature range 296–473K [*Perry et al*., 1977]. Most recently, Calvert et al. [2002] recommended the Arrhenius activation energy of □0.67 ± 0.16 kcal mol^{-1} over the temperature range 213–383 K. The literature activation energies are similar to our theoretical calculations using DFT, considering the respective uncertainties. The recent study by Uc et al. [2000] reported the activation energies between □3.13 and □4.99 kcal mol^{-1} with B3LYP/6-31G(d,p). Hence there is a significant difference in the calculated activation energies (in the range 1.6–1.8 kcal mol^{-1}) at the

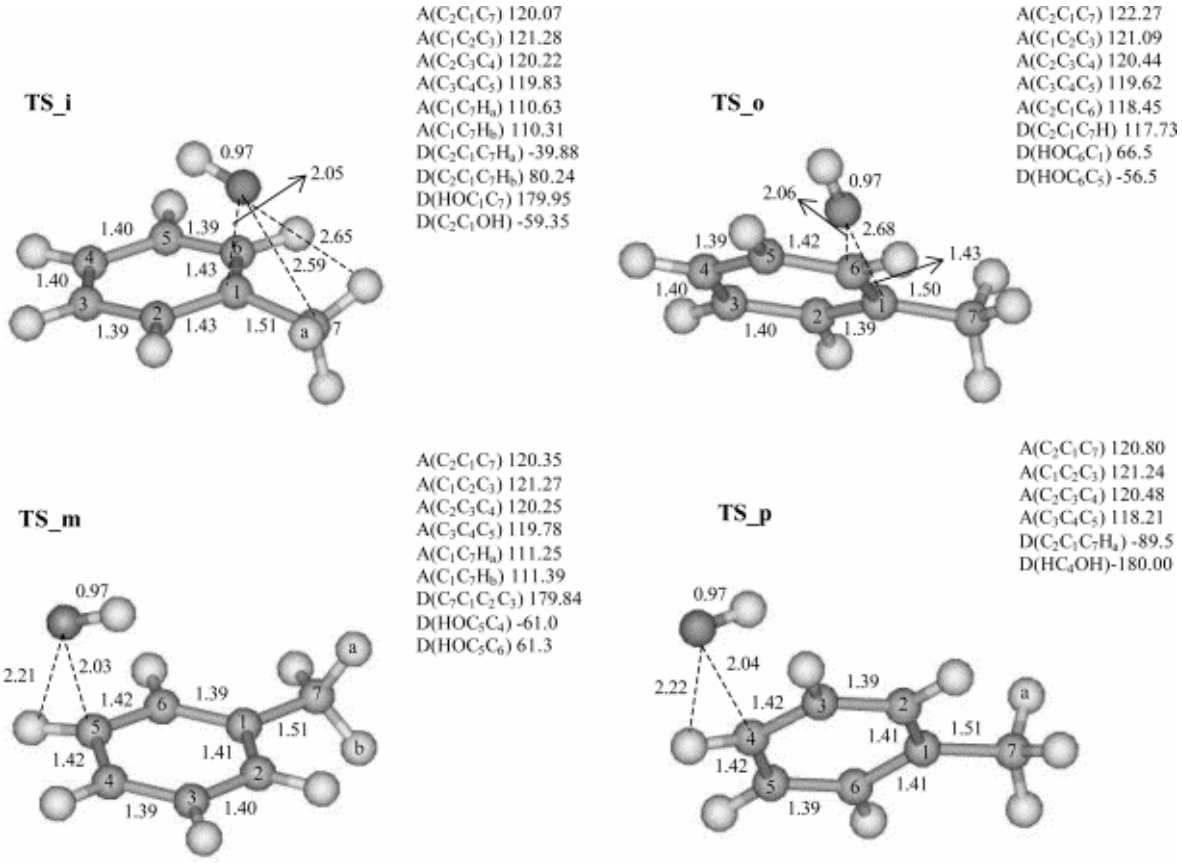

Figure 2.3. Optimized geometries of the transition states of the formation of the four isomers of the methyl hydroxycyclohexadienyl radicals calculated at the B3LYP/6-31G(d,p) level of theory (bond lengths in angstroms and angles in degrees).

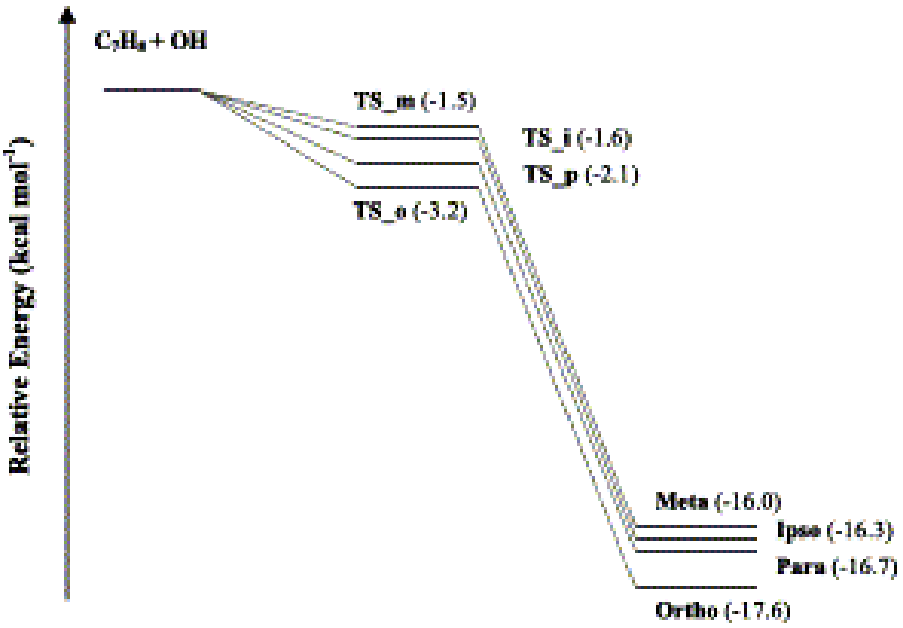

Figure 2.4. Potential energy surfaces (PES) of the isomers of the methyl hydroxycyclohexadienyl radicals relative to separated OH and toluene obtained at the B3LYP/6-31G(d,p) level of theory.

Table 2.3. TST calculated high-pressure limit recombination rate constant k_{rec} (cm^3 $molecule^{-1}$ s^{-1}), unimolecular decomposition rate constant k_{uni} (s^{-1}), branching ratios (*R*), and equilibrium constant *K* at 300 K.[a]

	k_{rec} (cm^3 $molecule^{-1}$ s^{-1})	k_{uni} (s^{-1})	R	K^b (molecule cm^{-3})
ipso	$3.4x10^{-13}$	$3.1x10^{2}$	0.03	$2.7x10^{4}$
ortho	$5.4x10^{-12}$	$3.9x10^{2}$	0.52	$3.4x10^{5}$
meta	$1.1x10^{-12}$	$7.9x10^{2}$	0.11	$3.5x10^{4}$
para	$3.5x10^{-12}$	$1.1x10^{2}$	0.34	$7.7x10^{5}$

B3LYP/6-31G(d,p) level of theory between the present study and the work of Uc et al. [2000].

2.3.3 Kinetic and Branching Ratio Calculations

The high-pressure rate constants for the formation of the methyl hydroxycyclohexadienyl radicals were calculated using the presently obtained activation energies and the transition state theory (TST) [*Lei and Zhang*, 2000]. The calculated high-pressure limit rate constants of OH addition to toluene and the corresponding isomeric branching ratios at 300 K are listed in Table 2.3. Using B3LYP/6-31G(d,p) we determined the rate constants in the range 3.4 x 10^{-13}–4.4 x 10^{-13} cm^3 $molecule^{-1}$ s^{-1}, with a total rate constant of 1.0 x10^{-11} cm^3 $molecule^{-1}$ s^{-1}. The rate constants predicted with B3LYP/6-311G(2df,2p) differ by less than 5%. The calculated ranching ratios using the various DFT methods are in the ranges 0.03–0.07 for the ipso isomer and 0.45–0.60 for the ortho isomer. On the other hand, the branching ratio for the ipso isomer predicted with CCSD(T)/6-31G(d)+CF method is considerably different, with a value of 0.31.

The rate constant of OH reaction with toluene has been reported by several experimental studies [*Knispel et al*., 1990; *Molina et al*., 1999; *Perry et al*., 1977; *Bourmada et al*., 1988]. A value of 5.63×10^{-12} cm^3 $molecule^{-1}$ s^{-1} at 299 K and 1 atm is recommended for atmospheric modeling [*Calvert et al*., 2002]. By fitting the observed OH decay in the presence of toluene using a triexponential expression, Knispel et al. reported an OH addition rate of (7.0 ± 2.1)×10^{-12} cm^3 $molecule^{-1}$ s^{-1} at 299 K. Our calculated total OH addition rate of 1.0×10^{-11} cm^3 $molecule^{-1}$ s^{-1} with B3LYP/6-31G(d,p)

agrees with the experimental values within a factor of 2. Since there are no adjustable parameters in calculating the TST rate constant, the success in reproducing the experimental rate suggests that the DFT energetics provide an accurate description of the salient features of the reaction. The unimolecular decomposition rate constant and equilibrium constant of the OH–toluene reaction are also summarized in Table 2.3 obtained by using the B3LYP/6-31G(d,p) energetics. The decomposition rate constants for the four isomers of the OH–toluene adduct range from 1.1×10^{2} to 7.90×10^{2} s^{-1}. The decomposition rate of the OH–toluene adduct was previously recommended as $9.4\times10^{12}\exp(-8540/T)$ s^{-1} [*Atkinson et al*., 1989].

Knispel et al. [1990] reported a decomposition rate constant of 4.8±1.8 s^{-1} at 299 K and 1 atm. Hence our calculated decomposition rates are substantially higher than the available literature values. Our calculated equilibrium constants at 1 atm indicate that unimolecular decomposition of the OH–toluene adduct is too slow to compete with bimolecular recombination.

2.4 Summary and Conclusions

Using B3LYP/6-31G(d,p) we determined the branching ratios of 0.52, 0.34, 0.11, 0.03 for the formation of *ortho*, *para*, *meta*, and *ipso* isomers, respectively, suggesting a strong preference for the *ortho* addition of OH to toluene. The work by Uc et al. [2000] determined the branching ratios of 0.04, 0.84, 0.05, and 0.07 for the formation of *ortho*, *para*, *meta*, and *ipso* isomers using B3LYP/6-31G(d,p). The differences between the two studies are attributable to the differences in the calculated activation energies. Using PMP2, Uc et al. [2000] obtained the branching ratios of 0.57, 0.40, 0.02, and 0.01 for

ipso, *ortho*, *meta*, and *para* isomers. The authors concluded that *ipso* addition of OH to toluene is most preferential, in disagreement with our present theoretical results. Several experimental studies have also inferred the branching ratios of the OH–toluene reaction on the basis of experimental studies of the cresol formation [*Smith et al*., 1998; *Klotz et al*., 1998]. Cresol formation arises from the initial addition of OH to the *ortho*, *meta*, and *para* positions followed by H-abstraction by O_2 molecules, but OH addition to the *ipso* position does not result in any cresol formation. The most recent study by Klotz et al. [1998] reported the product yields of 12.0±1.4%, 2.7±0.7%, and 3.2±0.6% for *o*-, *m*-, and *p*-cresol, respectively. Our predicted branching ratios using B3LYP/6-31G(d,p) are qualitatively similar to the experimental values. Hence the DFT method produces activation and reaction energies, rate constants, and isomeric branching ratios of the OH–toluene reaction in good agreement with the experimental values.

CHAPTER III

OXIDATION MECHANISM OF AROMATIC PEROXY AND BICYCLIC RADICALS FROM OH-TOLUENE REACTIONS*

Theoretical calculations have been performed to investigate mechanistic features of OH-initiated reactions of toluene. Aromatic peroxy radicals arising from initial OH and subsequent O_2 additions to the toluene ring are shown to cyclize to form bicyclic radicals rather than undergoing reaction with NO under atmospheric conditions. Isomerization of bicyclic radicals to more stable epoxide radicals possesses significantly higher barriers and hence has slower rates than O_2 addition to form bicyclic peroxy radicals. At each OH attachment site, only one isomeric pathway via the bicyclic peroxy radical is accessible to lead to ring cleavage. The study provides thermochemical and kinetic data for quantitative assessment of the photochemical production potential of ozone and formation of toxic products and secondary organic aerosol from toluene oxidation.

3.1 Introduction

As discussed in Chapter II, the OH-toluene reaction results in minor H-atom

* Reproduced with permission from Oxidation Mechanism of Aromatic Peroxy and Bicyclic Radicals from OH-Toluene Reactions, Suh, I., R. Y. Zhang, L. T. Molina, AND M. J. Molina, 2003, Journal of the American Chemical Society, 125, 12655-12665. Copyright 2003 American Chemical Society.

abstraction from the methyl group and major OH addition to the aromatic ring (about 90%) [*Calvert et al*., 2002; *Atkinson et al.*, 1997; *Seinfeld and Pandis*, 1998]. Under atmospheric condition the OH-toluene adduct reacts with O_2 either by O_2 addition to form (primary) peroxy radicals or by H-abstraction to yield phenolic compounds. The latter channel has been shown to be relatively minor, accounting for about 16% of the total products. The fate of the peroxy radicals is governed by competition between reaction with NO to form alkoxy radicals and cyclization to form bicyclic radicals. The bicyclic radicals can undergo unimolecular rearrangement to form epoxide radicals or bimolecular reaction with O_2 to form (secondary) bicyclic peroxy radicals. The mechanistic complexity of the toluene oxidation further arises from multiple isomeric pathways at each reaction stage. Initial OH addition to toluene results in four distinct structural OH-toluene adduct isomers (A1 to A4). Subsequent reactions of OH-toluene adducts with O_2 and cyclization of aromatic peroxy radicals also incur additional isomeric branching [*Garcia-Cruz et al*., 2000]. Schemes 1 and 2 illustrate the likely degradation pathways of toluene oxidation following OH addition to the ortho and para positions. For the ortho OH-toluene adduct, for example, O_2 addition to the aromatic ring occurs at C1, C3, or C5 on the ring, forming three possible structural isomers of the peroxy radicals. The next step involves formation of bicyclic radicals with an O-O bridge across the benzene ring, forming five possible isomers. The bicyclic radicals may isomerize to form eight possible epoxide radicals.

Scheme 1

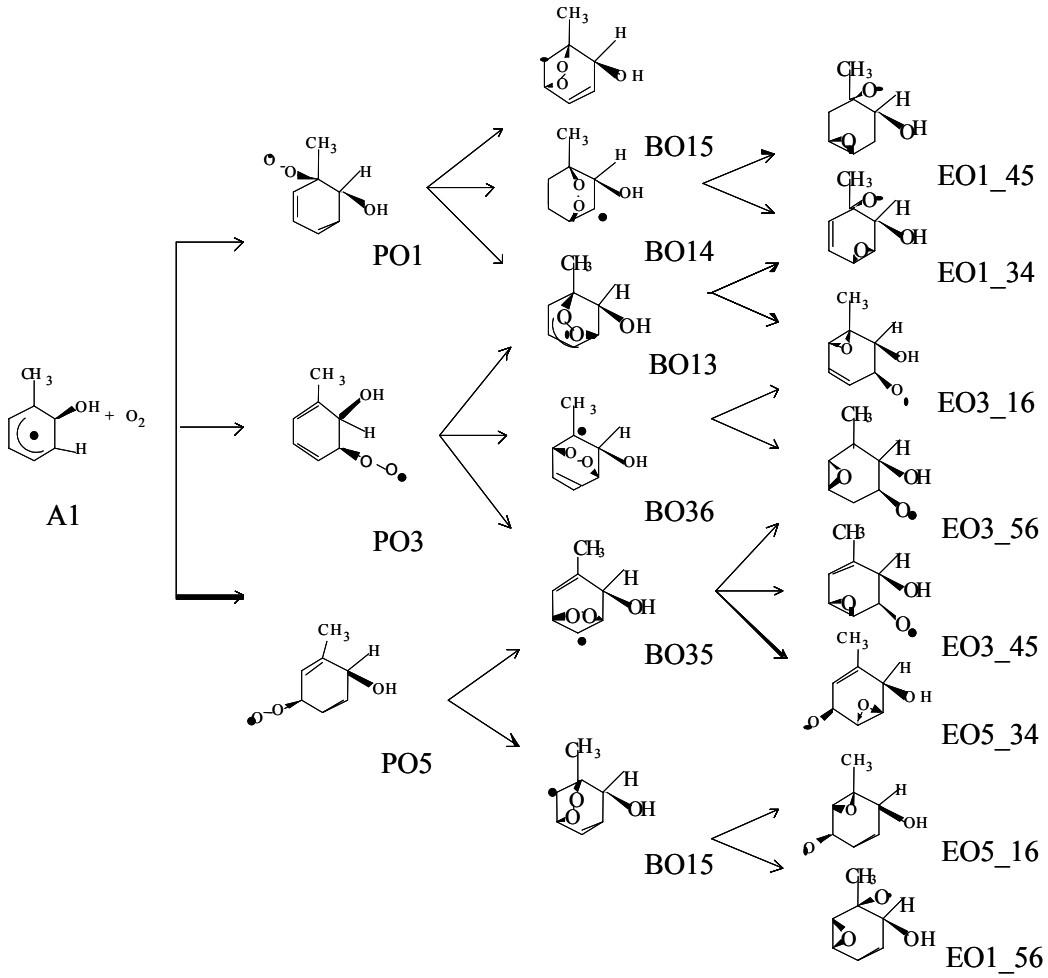
A1
PO1
PO3
PO5
BO15
BO14
BO13
BO36
BO35
BO15
EO1_45
EO1_34
EO3_16
EO3_56
EO3_45
EO5_34
EO5_16
EO1_56

Scheme 2

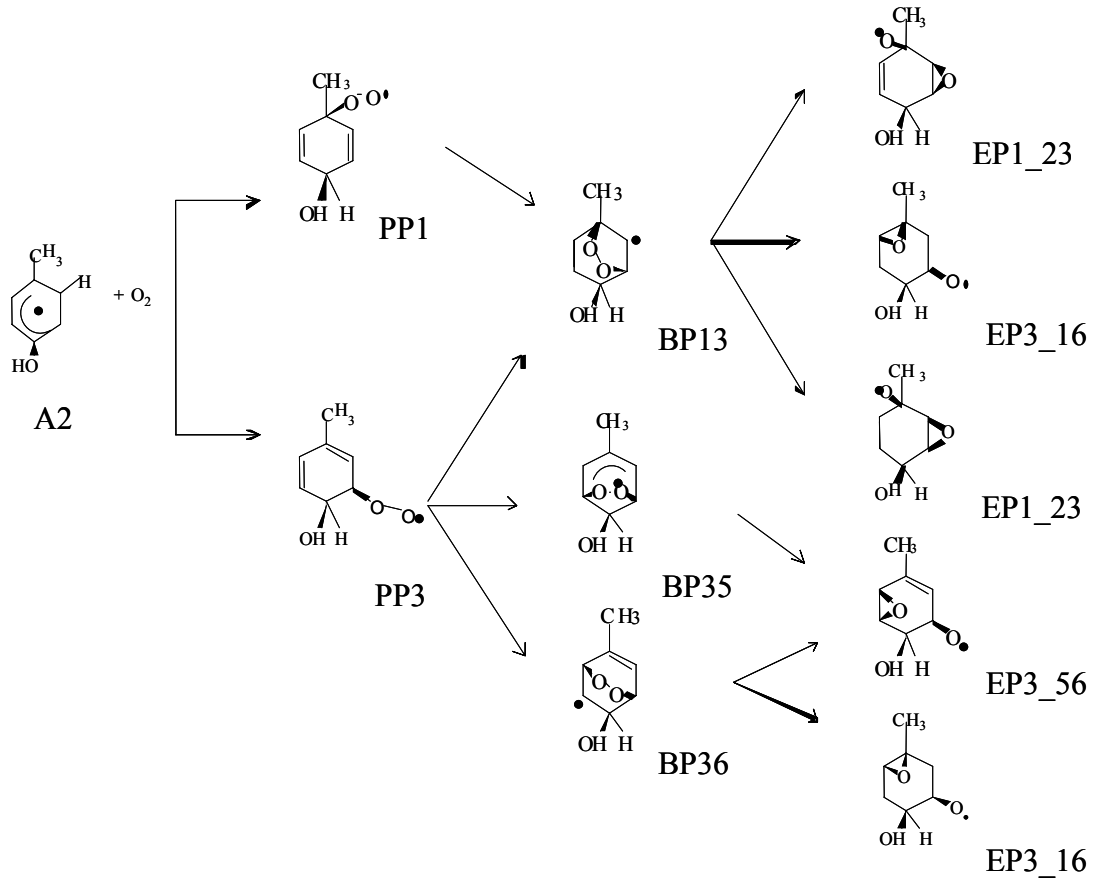

Environmental chamber studies have also identified several major products consisting of both ring retaining and fragmentation compounds [*Odum et al*., 1997; *Forstner et al*., 1997; *Yu et al*., 1997*; Shepson et al*., 1984; *Lonneman et al*., 1978; *Smith et al.*, 1998; *Klotz et al*., 1998; *Atkinson et al*., 1994; *Volkamer et al*., 2001]. In the presence of O_2 and NO_x, the identified reaction products include hydroxyl aromatic compounds, 2-, 4-, and 3-NO_2-toluene, along with ring cleavage products such as glyoxal, methylgloxal, and butenedial. The most abundant hydroxyl aromatic compound has been identified as o-cresol. A recent experimental study reported a significant yield (about 40 ± 10%) of glyoxal, and indicated that the ring-cleavage pathway involving the bicyclic peroxy radical represents the major pathway in the oxidation of monocyclic aromatic hydrocarbons [*Volkamer et al*., 2001]. In addition, it has been suggested that the major SOA components comprise unsaturated anhydrides resulting from ring cleavage [*Odum et al.*, 1997; *Forstner et al*., 1997].

Several theoretical studies have been performed to investigate the structures and energetics of the intermediate radicals from the OH-initiated oxidation of toluene, providing further insight into the mechanism of the OH-toluene reactions [*Garcia-Cruz et al*.2000; *Andino et al*, 1996; *Suh et al*., 2002].

In this Chapter, we report a theoretical study of the aromatic peroxy, bicyclic, epoxide, and bicyclic peroxy radicals from the OH-toluene reactions. Reaction energies for the formation of the aromatic radicals were obtained to determine their relative stability and reversibility, and activation barriers were analyzed to assess the energetically favorable pathways to propagate toluene oxidation. Kinetic calculations were performed using the classic transition state theory (TST) and RRKM/master

equation to assess the atmospheric degradation mechanism of the OH-toluene reaction system. Relevance of the present theoretical work to interpretation of available experimental product studies was emphasized.

3.2 Theoretical Methods

Quantum chemical computations were carried out similarly to those discussed in Chapter II. As discussed above, our recent work has evaluated the quantum chemical methods applicable to the aromatic intermediate radicals [*Suh et al*., 2002]. For the initial OH addition to toluene, we obtained the equilibrium structures and energetics of the OH-toluene adduct isomers and their corresponding transition states, using density function theory (B3LYP/6-31G(d,p)) and ab initio multiconfigurational calculations (CASSCF) for geometry optimization and second-order Møller-Plesset perturbation theory (MP2) and coupled-cluster theory (CCST(D)) for single-point energy calculations [*Suh et al*., 2002]. The results revealed that the DFT method predicted binding energies and activation energies in good agreement with the experimental values. The calculated rate constants and isomeric branching ratios for the formation of OH-toluene adducts using B3LYP/6-31G(d,p) structures and energetics were consistent with the experimental rate constant of the OH-toluene reaction and the measured cresol yields. On the other hand, the correlated methods employing MP2 and CCSD(T) produced significantly higher activation energies than the experimental value. The failure using the MP2 and CCSD(T) methods was explained by significant contamination of unrestricted Hartree-Fock wavefunction from higher spin states in the single-point energy calculations of the

transition states. The performance of CASSCF and CSSPT2 was also unsatisfactory, producing higher activation energies than the experimental value.

3.3 Results and Discussions

3.3.1 Primary Peroxy Radicals

O_2 addition to ortho OH-toluene adduct forms three possible structural isomers of the peroxy radicals (Scheme 1). Also, O_2 addition to the para OH-toluene adduct results in two plausible peroxy radical isomers. Figure 3.1 depicts the optimized geometries of the lowest-energy conformations of the peroxy radicals obtained using B3LYP/6-31G(d,p). The evaluation of the vibrational frequencies confirmed that all geometries reported represent minima on the potential energy surfaces.

For the peroxy radicals, the energetically favorable conformation corresponds to O_2 addition on the same side of the benzene ring as the hydroxyl group. Figure 3.1 shows that there exists intramolecular hydrogen bonding in the peroxy radicals. It involves interaction between the terminal oxygen of the peroxy group and the hydrogen of the OH group, forming a six-membered ring. The distance of intermolecular hydrogen bonding ranges from 1.90 to 1.95 Å.

Zero-point corrected reaction energies for the formation of the peroxy radicals are listed in Table 3.1, obtained at the B3LPY/6-31G(d,p) level of theory. Addition of O_2 to OH-toluene adducts leads to formation of the peroxy radicals with comparable relative stability within 2 kcal mol^{-1}. The binding energies of the peroxy radicals range from 3 to 6 kcal mol^{-1}. For the ortho OH-toluene adduct, O_2 addition at C3 of the aromatic ring represents the most stable isomer (**PO3**). It is clear that hydrogen bonding plays a role in stabilizing the peroxy radicals: the hydrogen bond lengths are 1.93, 1.90, and 2.33 Å for **PO1**, **PO3**, and **PO5**, respectively, correlating with their relative stability. To survey basis set and electronic correlation effects on the binding energies of the peroxy radicals, we performed additional calculations for **PO3** using several other methods, including MP2 and CCSD(T) for single-point energies and CASSCF and MPW1K for geometry optimization and energy calculations.

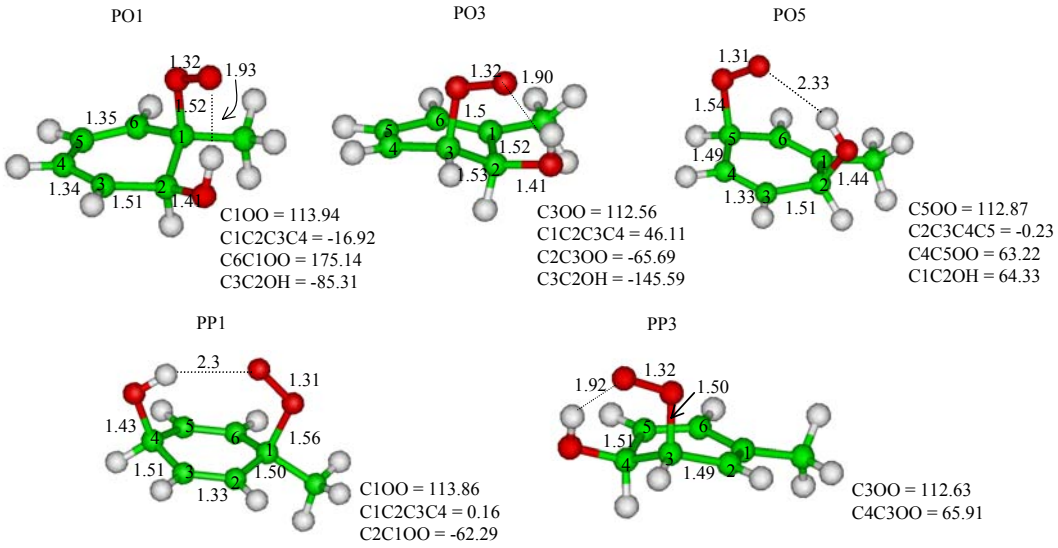

Figure 3.1. Structures of primary peroxy radicals at the B3LYP/6-31G(d,p) level of theory.

The results are provided in Table 3.2. The binding energies predicted by MPW1K and CASSCF are lower than that of B3LYP/6-31G(d,p), by 0.8 and 3.9 kcal mol^{-1}, respectively. On the other hand, the CCSD(T)/6-31G(d,p) method predicts a binding energy by 4.3 kcal mol^{-1} larger than the B3LYP/6-31G(d,p) value. Inclusion of the basis set correction method slightly reduces the difference between the CCSD(T)/6-31G(d) and B3LPY/6-31G(d,p) values. Spin contamination in the calculations of the peroxy radicals using the various quantum chemical methods is insignificant. The spin eigenvalues, $<S^2>$, are 0.760 for CCSD(T)/6-31G(d), 0.755 for MPW1K, and 0.75 for B3LYP/6-31G(d,p) before spin projection, nearly identical to the exact value of a pure doublet. Several previous theoretical studies have investigated OH-O_2-toluene peroxy radicals. Using a method involving semiempirical UHF/PM3 geometry optimization followed by B3LYP/6-31G(d,p) single-point energy calculations, Andino et al. [1996] considered the peroxy radicals with O_2 being added to the opposite side of the ring relative to the OH group and obtained the binding energies of about 3 to 5 kcal mol^{-1}. A recent study by Garcia-Cruz et al.[2000] investigated the configurations with O_2 being added to both the same and opposite sides of the ring relative to the OH group using B3LYP/6-31G(d) and PMP2 [*Garcia-Cruz et al.*, 2000]. The authors concluded the configuration with OH and O_2 on the same side of the ring results in a stabilization of 1.5 to 3.0 kcal mol^{-1} for the peroxy radicals. Our structures and binding energies of the peroxy radicals obtained by using B3LYP/6-31G(d,p) are consistent with those reported by Garcia-Cruz et al. using B3LYP/6-31G(d).

Table 3.1. Zero-point Corrected Reaction Energies (*RE* in kcal mol^{-1}) and Activation Energies (E_a in kcal mol^{-1}) for the OH-Toluene-O_2 Reaction System.[a]

Type	Reaction	*RE*	E_a
Ortho	**PO1**	-4.3	3.5
	PO3	-5.7	4.6
	PO5	-3.9	0.3
	PO5 → BO15	12.2	29.2
	PO1 → BO14	14.5	23.4
	PO1 → BO13 (a)	-8.0	9.0
	PO3 → BO13 (b)	-6.6	10.4
	PO3 → BO36	15.6	24.4
	PO5 →BO35	12.1	31.4
	BO14 →EO1_34	-36.7	
	BO13 → EO3_16	-16.6	16.4
	BO35 → EO5_34	-33.8	
	BO35 → EO3_45	-31.0	
	BO15 → EO5_16	-35.7	
	BO15 → EO1_56	-29.9	
	BO13 + O_2 → P_BO13_4	-13.7	2.0
	BO13 + O_2 → P_BO13_6	-12.9	2.1
Para	**PP1**	-4.0	-0.4
	PP3	-5.8	4.6
	PP1 → BP13	11.3	28.9
	PP3 → BP35	-6.4	10.7
	PP3 → BP36	14.8	23.7
	BP13 → EP1_23	-32.9	
	BP35 → EP3_56	-16.2	16.5
	BP35 + O_2 → P_BP35_2	-14.7	1.4

Table 3.1. (Continued)

Type	Reaction	*RE*	E_a
Ipso	**PI2**	-3.1	6.0
	PI4	-3.4	1.0
	PI2 → BI24	10.7	30.3
	PI2 → BI25	13.2	22.1
	PI2 → BI26	-9.0	9.5
	PI4 → BI46	11.6	29.6
	BI24 → EI2_34	-16.3	
	BI25 → EI2_45	-38.5	
	BI26 → EI2_56	-11.2	15.0
	BI45 → EI4_56	-34.6	
Meta	**PM2**	-5.6	5.0
	PM4	-5.7	5.2
	PM6	-6.1	

[a] All calculations were based on B3LYP/ 6-31G(d,p) optimized geometries. Zero-point energy (ZPE) corrections were calculated at the B3LYP/6-31G(d,p)//B3LYP/(6-31G(d,p).

Table 3.2. Binding Energies (D_o), Activation Energies (E_a), Rate Constants (k), Equilibrium Constants (K_{eq}) and Spin Eigenvalues ($<S^2>$) for peroxy radical **PO3** calculated using Various Quantum Chemical Methods.

Method	D_o	$< S^2 >$[a]	E_a	$< S^2 >$[b]	k (cm^3 molecule^{-1} s^{-1})	K_{eq} (cm^3 molecule^{-1})
B3LYP/6-1G(d,p)	5.7	0.75 (0.75)	4.6	0.98 (0.76)	1.1×10^{-17}	1.8×10^{-23}
CCSD(T)/6-31G(d)	10.0	0.76 (0.75)	11.3	2.14 (2.54)	1.7×10^{-22}	2.4×10^{-20}
CCSD(T)/6-31G(d) + CF	8.9		12.9		1.6×10^{-23}	3.8×10^{-21}
MPW1K[c]	4.9	0.76 (0.75)	11.7	1.30 (0.84)	6.8×10^{-23}	4.7×10^{-24}
CASSCF	1.8		9.5		2.7×10^{-21}	2.2×10^{-26}

[a] Spin Eigenvalues before (after) spin projection for the formation of **PO3**.
[b] Spin Eigenvalues before (after) spin projection for the transition state of **PO3**.
[c] Frequency calculations were based on MPWPW91/6-31G(d,p)//MPWPW91/6-31G(d,p).

Another theoretical study by Bartolotti and Edney calculated much larger binding energies for O_2 addition to the ortho OH-toluene adduct using density functional theory, ranging from 18 to 23 kcal mol^{-1} [*Bartolotti et al*., 1995]. For comparison, the binding energy of the analogous OH-benzene peroxy radical was predicted to be 8.2 and 5.2 kcal mol^{-1} using B3LYP/6-31(+)G(d) and B3LYP/6-311+G(d)//B3LYP/6-31(+)G(d), respectively [*Ghigo and Tonachini*, 1998]. Using a combined thermochemical group additivity rules and semiempirical UHF/PM3 method, Lay et al. obtained a slightly larger binding energy of 12 kcal mol^{-1} for the OH-benzene peroxy radical [*Lay et al*., 1996]. The transition state (TS) leading to the formation of the peroxy radical was searched by using TS keyword in geometry optimization at the B3LYP/6-31G(d,p) level of theory. The C-O bond length was successively increased relative to the equilibrium structures of the corresponding peroxy radical. Once an initial geometry optimization reached convergence, a frequency calculation was performed to determine whether this optimized geometry represented a first-order saddle point. A transition state was identified by finding only one imaginary component in the calculated vibrational frequencies. The vibrational modes along the reaction coordinates were examined to verify that these modes represented the trend along the intended reaction coordinate. At the B3LYP/6-31G(d,p) level of theory, we performed additional calculations using the intrinsic reaction coordinate (IRC) method, confirming that each TS uniquely connected the reactant to the product. The TS structures for the formation of peroxy radicals are illustrated in Figure 3.2. The C-O bond lengths at the transition

Table 3.3. Calculated High-Pressure Limit Rate Constants of the OH-Toluene-O_2 Reaction System at 300 K.[a]

Species	k_b (cm^3 $molecule^{-1}$ s^{-1})	k_{uni} (s^{-1})
PO1	$5.2x10^{-17}$	
PO3	$1.2x10^{-17}$	
PO5	$1.0x10^{-14}$	
BO13 (a)		$1.9x10^{6}$
BO13 (b)		$2.9x10^{4}$
EO3_16		6.8
P_BO13_4	$4.4x10^{-15}$	
P_BO13_6	$1.9x10^{-15}$	
PP1	$3.7x10^{-15}$	
PP3	$1.4x10^{-18}$	
BP35		$2.0x10^{4}$
EP3_56		4.5
P_BP35_2	$8.5x10^{-15}$	
P12	$8.1x10^{-19}$	
BI26		$9.2x10^{4}$
EI2_56		$1.8x10^{2}$

[a] Using B3LYP/6-31G(d,p) results.

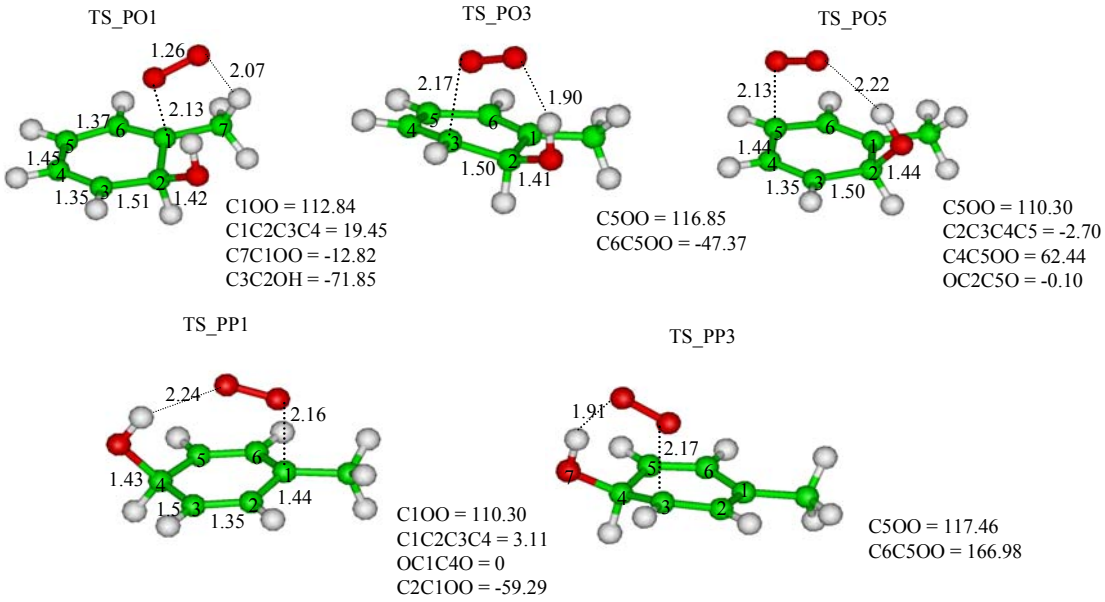

Figure 3.2. TS structures of primary peroxy radicals at the B3LYP/6-31G(d,p) level of theory.

states range from 2.13 to 2.17 Å. Intramolecular hydrogen bonding also exists in the TS structures. The hydrogen bond lengths are between 1.88 to 2.24 Å, with the latter value corresponding to rather weak hydrogen bonding. The activation energies to form the peroxy radicals are also included in Table 3.1. The activation barriers of O_2 addition to the ortho OH-toluene adduct are less than 5 kcal mol^{-1}. It is interesting to note that, although the peroxy radical **PO3** represents the most stable form for ortho OH addition, its activation energy is slightly higher than those of **PO1** and **PO5**. We also examined basis set and electronic correlation effects on the barrier heights for **PO3** in Table 3.2. The CCSD(T)/6-31G(d) and CCSD(T)/6-31G(d) + CF methods both predict higher activation energies than the B3LYP/6-31G(d,p) method, by 6.7 and 8.3 kcal mol^{-1}, respectively. The MPW1K and CASSCF barrier heights are also higher than the B3LYP value, but are slightly less than the CCSD(T) values. Spin contamination in calculating the TS energy using CCSD(T) is significant, with the $<S^2>$ value of 2.13 before the S + 1 component is annihilated, rendering this method unreliable. The MPW1K method also suffers from spin contamination with a $<S^2>$ value of 1.26 before annihilation. For the B3LYP/6-31G(d,p) method, the $<S^2>$ values are 0.98 and 0.76 before and after annihilation, respectively. It should be pointed out that calculations of geometries and energetics of the transition states of the peroxy radicals using CASSCF and CCSD(T) are computationally extremely consuming, and it is unrealistic to employ both methods for each species investigated in this work. The study by Andino et al. [1996] reported the activation barriers of 8 to 10 kcal mol^{-1} for the OH-toluene peroxy radicals, higher than our B3LYP/6-31G(d,p) values.

We calculated the high-pressure rate constants of O_2 addition to the OH-toluene adducts, using the classic transition state theory (TST) and the structures and energetics obtained with B3LYP/6-31G(d,p). As presented in Table 3.3, the calculated rate constants range from 10^{-14} to 10^{-18} cm^3 $molecule^{-1}$ s^{-1}, showing distinct kinetics for the isomers of the peroxy radicals. For the ortho OH adduct, O_2 addition occurs with the rate constants of 5.2 x 10^{-17}, 1.2 x 10^{-17}, and 1.0 x 10^{-14} cm^3 $molecule^{-1}$ s^{-1} for **PO1**, **PO3**, and **PO5**, respectively. Several experimental studies have reported the O_2 addition rate to the OH-toluene adduct [*Knispel et al*., 1990; *Bohn*, 2001]. Early studies indirectly inferred this rate by fitting OH decay in the presence of toluene and O_2 and assuming a tri-exponential formulation, with the rate constant of (5 – 6) x 10^{-16} cm^3 $molecule^{-1}$ s^{-1} at room temperature [*Knispel et al*., 1990]. A more recent work by Bohn investigated the kinetics of the OH-toluene adduct with O_2 by monitoring the OH-toluene adduct using cw UV-laser long path absorption, and reported a larger rate constant of (3 ± 2) x 10^{-15} cm^3 $molecule^{-1}$ s^{-1} [*Bohn*, 2001]. Our calculated rate constants of the reactions of the OH-toluene adducts with O_2 encompass the previous experimental values, but suggest strong isomeric and multi-exponential kinetic effects which are unaccounted for in the previous experimental studies. It is also clear from Table 3.2 that the activation barriers predicted by CCSD(T), MPW1K, and CASSCF are significantly higher, yielding much lower rate constants than the experimental values. Apparently, the CCSD(T) method produces erroneous activation barriers because of significant spin contamination. Equilibrium between formation and decomposition of the peroxy radicals was evaluated according to eq. 2. Using the

B3LYP/6-31G(d,p) results, the calculated equilibrium constants range from 10^{-23} to 10^{-24} cm^3 $molecule^{-1}$ for the peroxy radicals with ortho and para OH additions. The equilibrium constants of **PO3** predicted by the various methods are contained in Table 3.2. The CCSD(T) methods yield the largest equilibrium constants of 2.4 x 10^{-20} cm^3 $molecule^{-1}$ with CCSD(T)/6-31G(d)) and 3.8 x 10^{-21} cm^3 $molecule^{-1}$ with CCSD(T)/6-31G(d) + CF. The recent experimental work by Bohn reported an equilibrium constant of (3.25 ± 0.33) x 10^{-19} cm^3 $molecule^{-1}$ for OH-O_2-toluene peroxy radicals [*Bohn*, 2001]. The experimental equilibrium constant is significantly higher than our B3LYP/6-31G(d,p) value, but is closer to our CCSD(T) values. Note that our results reveal that the binding energies of the peroxy radicals differ by 3 kcal mol^{-1} in Table 3.1. As reflected by eq. 2, the equilibrium constant is strongly dependent on binding energies of the peroxy radicals, and the equilibrium constants of the peroxy radical isomers differ significantly (by two to three orders of magnitude). The result reported in the previous experimental study by fitting the experimental data assuming a single equilibrium constant is likely inaccurate. Due to the relatively small binding energies of the peroxy radicals, the OH-toluene adduct reaction with O_2 proceeds reversibly and the equilibrium favors peroxy radical decomposition. The close relative stability and reversibility of the peroxy radicals suggest that all isomers of the peroxy radicals are likely to form. The relative stability and activation barriers of the peroxy radicals, however, have little effect on isomeric branching, since propagation of the toluene oxidation is largely determined by the exit channel of the peroxy radicals.

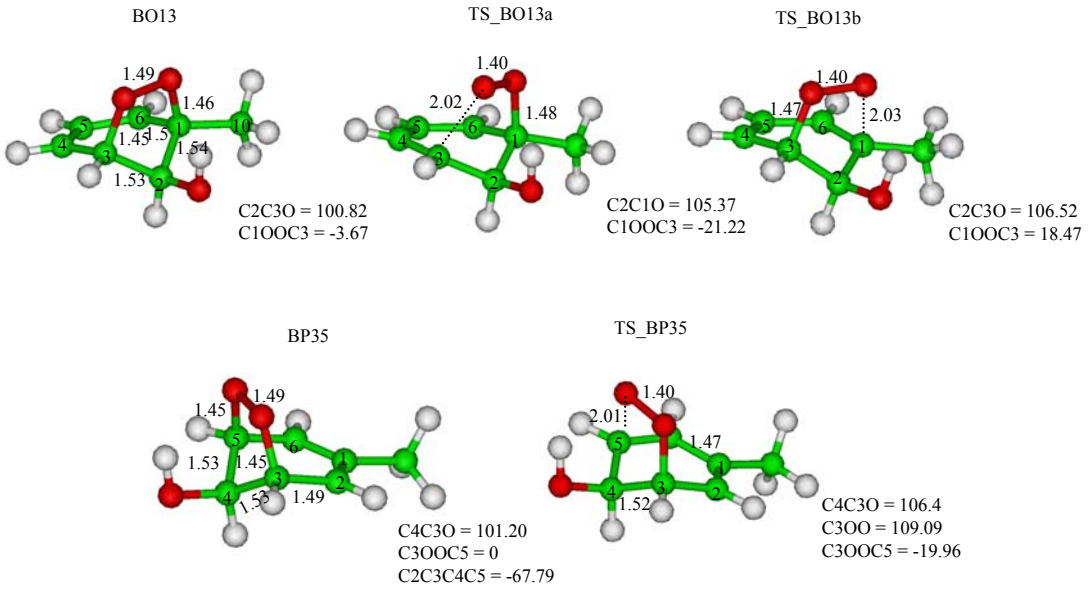

Figure 3.3. Structures of bicyclic radicals and their corresponding transition states at the B3LYP/6-31G(d,p) level of theory.

The steady-state concentrations of the peroxy radicals are determined by recombination of the adduct with O_2, dissociation of the peroxy radicals, and the exit channel of the peroxy radicals, that is, reaction with NO to form alkoxy radicals or rearrangement to form bridged bicyclic radicals.

3.3.2 Bicyclic Radicals

For ortho OH addition, peroxy radicals **PO1** and **PO3** each likely cyclize to form three possible bridged bicyclic radicals, and peroxy radical **PO5** likely cyclizes to form two possible bicyclic radicals. Also, cyclization of **PO1** and **PO3** (**PO3** and **PO5**) leads to an identical bicyclic radical **BO13** (**BO35**). Formation of **BO13** from **PO1** and **PO3** involves a five-membered oxygen ring, with initial O_2 attachment to a tertiary and secondary site and subsequent C-O closure to a secondary and tertiary site, respectively. Hence there exist six plausible bicyclic radicals from ortho OH addition. Similarly, three possible bicyclic radicals are resulted from para OH addition. Figure 3.3 shows the equilibrium structures and transition states for bicyclic radicals **BO13** and **BP35**. The TS structures leading to **BO13** formation from **PO1** and **PO3** are similar, with the exception of the bridged C-O bond distances and the dihedral angle C1OOC3. The distances for C-O closure at the transition states are 2.02 and 2.03 Å for **PO1** and **PO3**, respectively. The reaction and activation energies for isomerization of peroxy to bicyclic radicals are presented in Table 3.1. The potential energy surface (PES) of the peroxy to bicyclic radical isomerization is illustrated in Figure 3.4.

The results from Table 3.1 and Figure 3.4 indicate that unlike the primary peroxy radicals the bridged bicyclic radicals exhibit distinct stability patterns. For ortho

OH addition, the bicyclic radical formed by O_2 addition at C1 and subsequent bridge formation at C1 and C3 (**BO13**) is most stable, while the other bicyclic radicals possess structures that are about 20 kcal mol^{-1} higher in energy. Similarly, for para OH addition, the bicyclic radical **BP35** represents the most stable form, and is located about 20 kcal mol^{-1} below its other two structural isomers. The high stability of **BO13** and **BP35** is explained since both structures possess a delocalized allyl-π system, while their other structural isomers possess only one localized double bond [*Garcia-Cruz et al*., 2000; *Andino et al*., 1996].

Formation of the nonallylically stabilized bicyclic radicals occurs *via* high-lying transition states and the activation barriers are 10 to 20 kcal mol^{-1} higher than those of **BO13** and **BP35**. At the B3LYP/6-31G(d,p) level of theory, isomerization of **PO3** to **BO13** is exothermic by about 7 kcal mol^{-1} and occurs with an activation barrier of about 10 kcal mol^{-1}. The exothermicity and activation barrier for **BO13** from **PO1** are both about 1.4 kcal mol^{-1} less than those from **PO3**. The reaction and activation energies of **BP35** are very similar to those of **BO13**. The previous theoretical work by Andino et al. [1996] reported the activation energies of 17.2 and 12.4 kcal mol^{-1} for isomerization of **PO3** and **PO1** to **BO13**, respectively, 6.9 and 3.4 kcal mol^{-1} higher than our B3LYP/6-31G(d,p) values [*Andino et al*., 1996]. Our additional calculations using CASSCF, CCSD(T)/6-31G(d,p), and CCSD(T)/6-31G(d,p) + CF yielded slightly higher activation energies of **PO3** to **BO13** isomerization, but these results are within 2.7 kcal mol^{-1} of the B3LYP/6-31G(d,p) barrier height (Table 3.4). In addition, except for the CASSCF method which predicts a higher stability, the reaction energies predicted

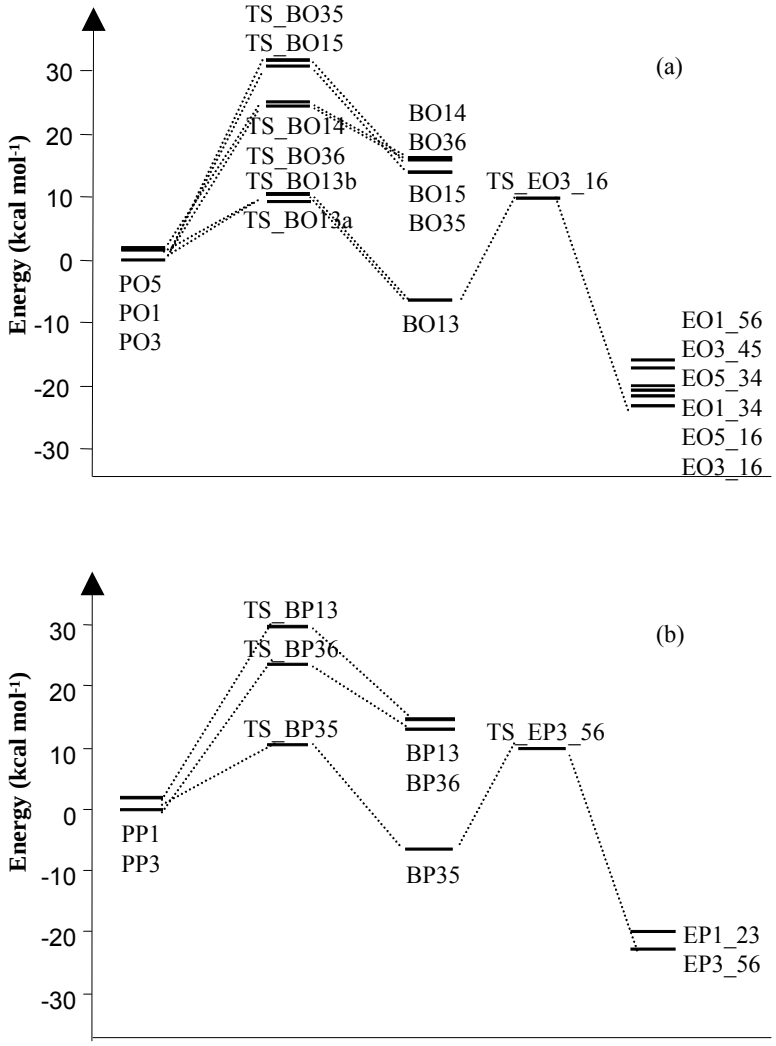

Figure 3.4. Potential energy surface (PES) involving primary peroxy, bicyclic, and epoxy radicals for ortho (a) and para (b) OH addition obtained by using B3LYP/6-31G(d,p).

Table 3.4. Calculations of Reaction Energies (*RE*), Activation Energies (E_a) for the Formation of Bicyclic **BO13** and Epoxide **EO3_16**.

Reaction	CASSCF		CCSD(T)/6-31G(d)		CCSD(T)/ 6-31G(d) + CF	
	RE	E_a	*RE*	E_a	*RE*	E_a
PO3 → **BO13**	-27.2	12.2	-10.5	12.5	-9.7	13.1
BO13 → **EO3_16**	-24.6	19.6	-18.2	28.0	-19.1	27.3

by the CCSD(T) methods are within 4 kcal mol^{-1} of the B3LYP/6-31G(d,p) value. Spin contamination associated with calculations of the bicyclic radicals and their corresponding TSs using the B3LYP/6-31G(d,p) method is minimal: for **BO13** the $<S^2>$ values are 0.78 and 0.75 before and after spin projection, respectively. At the CCSD(T)/6-31G(d) level of theory, the $<S^2>$ values before (after) spin projection are 0.937 (0.759) for **BO13** and 1.333 (0.958) for its corresponding TS.

Since the reaction of the OH-toluene adduct with O_2 is exoergic, the peroxy radicals produced are vibrationally excited. There are three possible reaction pathways for the excited peroxy radicals: collisional stabilization, prompt isomerization to the bicyclic radical, or prompt dissociation to the OH-toluene adduct. We performed calculations to assess the fate of the excited peroxy radicals using the RRKM/master equation (ME) formalism. The master equation analysis predicted predominant stabilization for the peroxy radicals, with a negligible fraction for prompt unimolecular reactions. The dominance of stabilization for the peroxy radicals is not surprising, considering the nearly identical barrier heights between cyclization to the bicyclic radicals and decomposition to the OH-toluene adducts.

Using the B3LYP/6-31G(d,p) results, we calculated the rate constants of 3×10^4 and 1.9×10^6 s^{-1} for isomerization of thermalized **PO3** and **PO1** to **BO13**, respectively. Formation of bicyclic radical **BP35** has a rate of 2.0×10^4 s^{-1}. In the atmosphere, there are two competing reactions for the primary peroxy radicals, i.e., isomerization to bicyclic radicals or reaction with NO to form alkoxy radicals and NO_2. We estimated a first-order rate constant of about 2 s^{-1} for the peroxy radical with NO, assuming a rate constant on the order of 10^{-11} cm^3 $molecule^{-1}$ s^{-1} for the NO-peroxy radical reaction and

an ambient NO mixing ratio of 10 ppb typical of a polluted urban atmosphere [*Calvert et al*., 2002; *Atkinson et al.,* 1997; *Seinfeld and Pandis*, 1998]. Isomerization of peroxy radical **PO1** or **PO3** to bicyclic radical **BO13** is significantly faster than the competing reaction with NO. The dominance of the bicyclic radical formation over the alkoxy radical formation from the primary peroxy radicals remains unchanged, even if the CASSCF or CCSD(T) results are considered. Furthermore, the decomposition rate of **PO1** or **PO3** to the OH-toluene adduct is comparable to that of isomerization to the bicyclic radical, due to nearly identical activation barriers. Hence, despite the likely existence of all primary peroxy radical isomers, formation of bicylic radical **BO13** is only allowed, and is contributed by peroxy radicals **PO1** and **PO3**. Isomerization of the peroxy radical to bicyclic radical **BO13** represents the only accessible isomeric pathway to propagate toluene oxidation for ortho OH addition. Similarly, for para OH addition, only the peroxy radical **PP3** is able to cyclize to form the bicyclic radical **BP35**, and the peroxy radical cyclization dominates over the reaction with NO.

The previous experimental study by Bohn observed an irreversible loss of the OH-toluene adduct that could not be interpreted by simply considering the equilibrium between the adduct and peroxy radicals [*Bohn*, 2001]. The author attributed this loss to two possible pathways, i.e., an additional irreversible reaction of the adduct with O_2 with a bimolecular rate constant of $(6.0 \pm 0.5) \times 10^{-16}$ cm^3 $molecule^{-1}$ s^{-1} and a unimolecular rate of $(1.85 \pm 0.15) \times 10^3$ s^{-1} for the peroxy radical. Our calculated rate constants for the exit channel of the peroxy radical, that is the formation of the bicyclic radical, are apparently consistent with the experimentally proposed unimolecular rate, considering the respective uncertainties.

3.3.3 Epoxy Radicals

The high-lying transition states and unstable structures of the nonallylic bicyclic radicals render formation of the majority of the epoxy radicals atmospherically irrelevant (Schemes 1 and 2). For ortho OH addition, only the formation of epoxides **EO1_34** and **EO3_16** are plausible, both resulting from isomerization of **BO13**. For the para OH adduct, isomerization of bicyclic radical **BP35** leads to epoxide **EP3_56**. The equilibrium structures of epoxides **EO3_16** and **EP3_56** are shown in Figure 3.5, along with their corresponding transition states. At the transition states, the distances for breaking the O-O bond are 1.88 Å for **EO3_16** and 1.90 Å for **EP3_56**, and the distances for C-O closure are 2.15 Å for **EO3_16** and 2.17 Å for **EP3_56**. The relative stability of the epoxy radicals and the PSE for bicyclic to epoxy radical isomerization are also shown in Figure 3.4.

The epoxy radicals are mostly noticeable for their high stability. The epoxides are about 16 to 37 kcal mol^{-1} more stable than their bicyclic precursors and about 16 to 23 kcal mol^{-1} more stable than their peroxy radical precursors (Table 3.1). For ortho OH addition, the epoxide **EO3_16** is most stable, and the relative stability of the epoxides are within 7 kcal mol^{-1}. Epoxide **EP3_56** is most stable for para OH addition. The activation barrier of **EO3_16** from **BO13** is predicted to be 16.4 kcal mol^{-1}. We were unable to locate the transition state for **EO1_34** from **BO13**, but it is expected that the activation barrier for this epoxide is higher than that for **EO3_16**. Epoxide **EO1_34** is about 3 kcal mol^{-1} less stable than **EO3_16**. Isomerization of **BP35** to **EP3_56** has a comparable barrier of 16.5 kcal mol^{-1}.

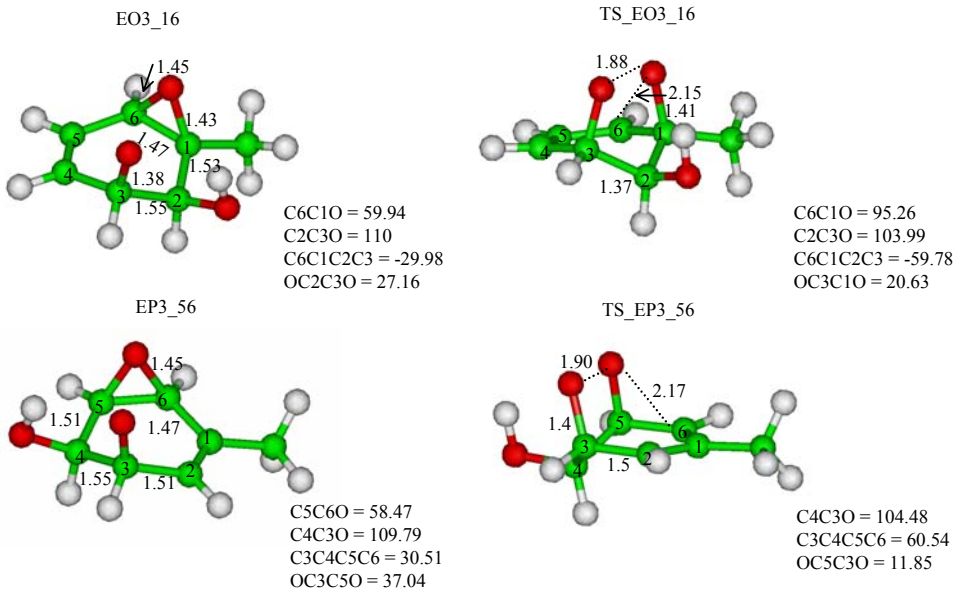

Figure 3.5. Structures of epoxy radicals and their corresponding transition states at the B3LYP/6-31G(d,p) level of theory.

The activation barrier is about 3 kcal mol^{-1} higher with CASSCF and 10 to 11 kcal mol^{-1} with CCSD(T). Spin contamination associated with the B3LYP/6-31G(d,p) method is unimportant for the epoxy radicals, with the $<S^2>$ value very close to 0.75 before projection. The $<S^2>$ value with CCSD(T)/6-31G(d) for **EO3_16** is 0.86 (0.75) before (after) projection. However, spin contamination is of concern in the TS calculation of **EO3_16** using CCSD(T), with the $<S^2>$ of 1.90 and 1.46 before and after projection, respectively.

Due to the higher activation barriers, the calculated high-pressure limit rate constants for isomerization of the thermalized bicyclic radical to epoxide are small, ranging from 4 to7 s^{-1} in Table 3.3. Those rate constants are even smaller, if the activation barriers predicted by CASSCF and CCSD(T) are considered in Table 3.4. Also, the RRKM/ME formalism was employed to assess the fate of chemically excited bicyclic radicals. The calculations suggested dominant stabilization for the bicyclic radicals, with a negligible fraction of prompt unimolecular reactions to the primary peroxy radicals or epoxy radicals.

3.3.4 Bicyclic Peroxy Radicals

For ortho OH addition, we considered two bicyclic peroxy radicals, with O_2 addition at C4 and C6 to **BO13**, denoted as **P_BO13_4** and **P_BO13_6**, respectively. For para OH addition, the bicyclic peroxy radical, **P_BP35_2**, with O_2 addition to C2 to **BP35** was investigated. Geometry optimization and energy calculations of the bicyclic peroxy radicals were only performed using the B3LYP/6-31G(d,p) method. The

equilibrium structures for the bicyclic peroxy radicals and their corresponding transition states are shown in Figure 3.6. The PSE for the bicyclic peroxy radicals is shown in Figure 3.7. The bicyclic peroxy radicals **P_BO13_4** and **P_BO13_6** are 12.9 and 13.7 kcal mol^{-1} more stable than **BO13** and their activation barriers are 2.1 and 2.0 kcal mol^{-1}, respectively. The reaction and activation energies of **P_BP35_2** are comparable, with the values of 14.7 and 1.4 kcal mol^{-1}, respectively. The binding energies of the bicyclic peroxy radicals are substantially larger than those of the primary peroxy radicals at the B3LYP/6-31G(d,p) level of theory. Spin contamination for the bicyclic peroxy radicals are minimal using B3LYP/6-31G(d,p). Spin contamination in the TS calculations of the bicyclic peroxy radicals is non-negligible, but is effectively removed after spin project.

The calculated bimolecular rate constants for the formation of the bicyclic peroxy radicals range from 2 x 10^{-15} to 9 x 10^{-15} cm^3 $molecule^{-1}$ s^{-1} in Table 3.3. O_2 addition to the bicyclic radical **BO13** to form **P_BO13_4** occurs about two times faster than that to form **P_BO13_6**.

3.3.5 Fate of Bicyclic Radicals: Isomerization *vs* O_2 Reaction

We now discuss the fate of the bicyclic radicals, i.e., the competition between isomerization to epoxides and O_2 addition to form bicyclic peroxy radicals. For both ortho and para addition pathways, isomerization of bicyclic radicals yields epoxide radicals which are slightly more stable than the bicyclic peroxy radicals in Figure 3.7. However, the activation barriers leading to the epoxides are significantly higher. The

effective first-order rate constants of the reaction of bicyclic radicals with O_2 are (1 – 5) x 10^4 s^{-1}. Consequently, the O_2 addition rate to form the bicyclic peroxy radical is nearly four orders of magnitude faster than that of epoxide formation, indicating that bicyclic radicals react exclusively by bimolecular reaction with O_2. The bicyclic peroxy radicals are then expected to react with NO to form the bicyclic alkoxy radicals and NO2, which is important for ozone formation. The bicyclic alkoxy radicals subsequently undergo ring cleavage, leading to formation of glyoxal and methyl glyoxal along with several unsaturated anhydrides (dihydro-2,5,-furandione, 2,5-furandione, and 3-methyl-2,5-furandione) which have been detected as the primary SOA components [*Seinfeld et al*., 1997; *Odum et al*., 1997; *Forstner et al*., 1997]. The previous theoretical work by Lay et al. also assessed the formation of bicyclic radicals and bicylic peroxy radicals from OH-benzene using the semiempirical UHF/PM3 method. The formation of epoxides was initially suggested because of their high stability [*Bartolotti et al*., 1995]. On the basis of an environmental chamber study of the OH-initiated reactions of several alkylbenzenes using GC/MS detection, Jeffries and coworkers detected several mass peaks matching those of epoxide carbonyls [*Yu et al*., 1997]. The yields of those products, however, were observed to be small. Also, the authors suggested that positive identification of the epoxy carbonyls in actual experimental conditions required authentic standards. Hence, experimental evidence for the formation of epoxide radicals was rather inconclusive.

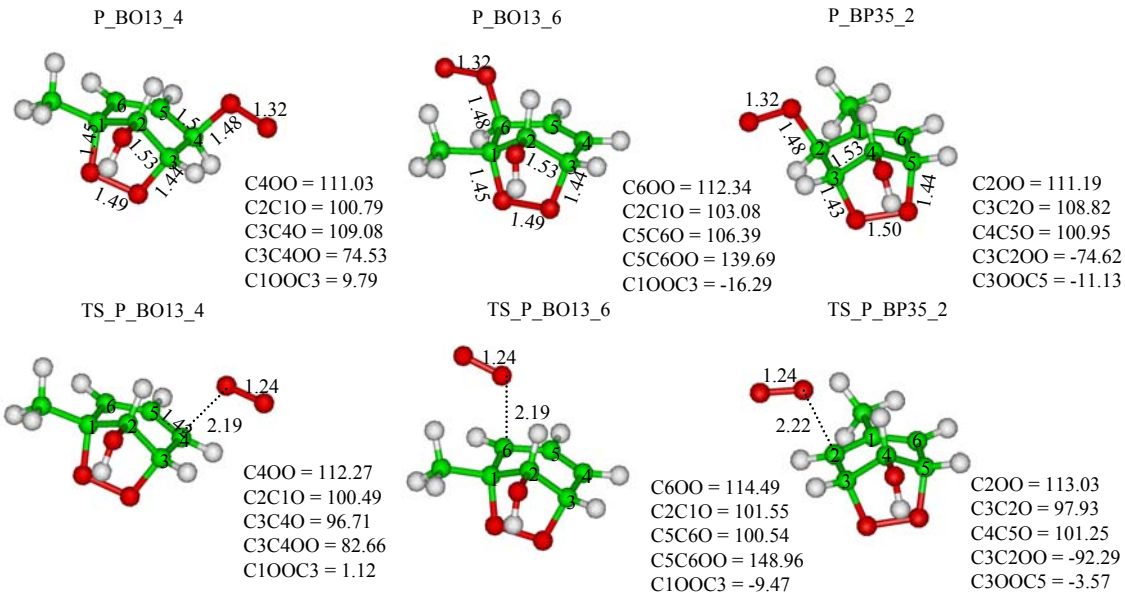

Figure 3.6. Structures of bicyclic peroxy radicals and their corresponding transition states at the B3LYP/6-31G(d,p) level of theory.

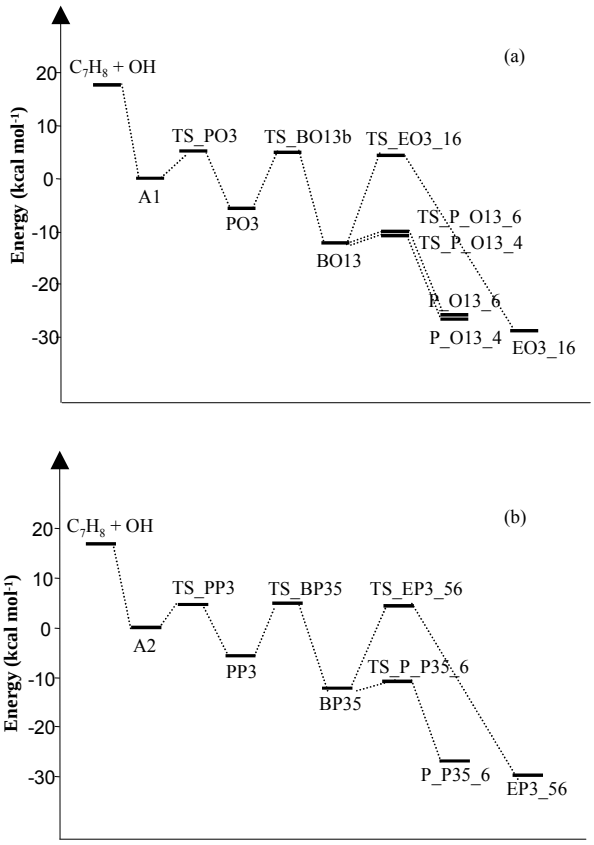

Figure 3.7. Potential energy surface (PES) of the OH-toluene reaction system for ortho (a) and para (b) OH addition obtained by using B3LYP/6-31G(d,p).

Recently, Volkamer et al. [2001] investigated primary versus secondary glyoxal yields. Their measurement of time-resolved glyoxal yield allowed for differentiation of primary and secondary glyoxal formation. Although glyoxal can be in principle produced from degradation of many intermediates including alkoxy, bicyclic peroxy, and epoxide radicals, only the pathway *via* the bicyclic peroxy radical leads to the primary formation on a relatively short time scale. The experimental study showed dominant primary glyoxal formation, with a yield of (39.0 ± 10.2)%. Hence the experimental evidence suggests that the ortho addition pathway proceeds primarily *via* the bicyclic peroxy radical channel, in agreement with our theoretical prediction. A more recent theoretical work also suggested the non-plausibility of epoxide formation from oxidative degradation of benzene [*Lin et al*., 2002].

In Chapter II we predicted the branching ratios of OH addition to ortho, para, meta, and ipso positions to be 0.52, 0.34, 0.11, and 0.03, respectively, indicating a strong preference of OH addition to the ortho and para positions. Using those branching ratios along with the kinetic results from this work, we estimated the yield for glyoxal formation. Our estimate of the glyoxal yield required data on cresol formation, which were on the basis of the experimental studies, with a total yield of about 18% [*Shepson et al*., 1984; *Lonneman et al*., 1978; *Smith et al.*, 1998; *Klotz et al*., 1998; *Atkinson et al*., 1994]. Cresol formation occurs either by H-abstraction by O_2 from the OH-toluene adduct or by HO_2 elimination from the peroxy radicals. We predicted a glyoxal yield of less than 50%, consistent with the experimental observation by Volkamer et al. [2001].

3.4 Summary and Conclusions

The present theoretical results provide new insights into the mechanism of toluene oxidation in the atmosphere. The thermochemical and kinetic data allow for a quantitative assessment of the formation potential of ozone, epoxide carbonyls, and SOA. The results explain previous product observations and provide guidance for future experimental and field studies to identify intermediates, stable products, and SOA components from the oxidation of toluene in the atmosphere. Our work confirms previous experimental and theoretical studies on the reversibility of the reaction of the OH-toluene adduct with O_2. The results, however, suggest strong isomeric effects on the rate constants and equilibrium constants for this reaction. The relative stability and activation barriers of the peroxy radicals have negligible effect on isomeric branching of the OH-toluene reactions. Ozone production from the primary peroxy radicals is unimportant, since the peroxy radicals mainly cyclize to produce the bicyclic radicals rather than react with NO. At each OH attachment site, only one isomeric pathway via the bicyclic peroxy radical is accessible to lead to ring cleavage. Rearrangement of bicyclic radicals to more stable epoxides is too slow to matter because of the high activation barriers, and we conclude that there is negligible formation of epoxide carbonyls from the epoxide intermediates.

CHAPTER IV

THEORETICAL STUDY OF BICYCLIC ALKOXY RADICALS AND THEIR DECOMPOSITION PATHWAYS

Theoretical calculations have been performed to investigate the bicyclic alkoxy radicals and their decomposition pathways. The reaction energies of the acyclic radicals op_4O and op_6O are 47.79 and 55.18 kcal mol^{-1} more stable than those of the bicyclic alkoxy radicals alc_4o and alc_6o and their corresponding activation barriers are 7.3 and 4.2 kcal mol^{-1}, respectively. The decomposition of the acyclic radicals leads to the formation of the SOA precursors such as the glyoxal, methyl glyoxal, and dicarbonaly compounds.

4.1 Introduction

As discussed in Chapter III, the bicyclic peroxy radicals react with NO to form the bicyclic alkoxy radicals and NO_2. The bicyclic alkoxy radicals undergo ring fragmentations to yield the acyclic radicals, which are subsequently decomposed to form the final products. Scheme 3 illustrates the mechanisms for the unimolecular decompositions of the bicyclic alkoxy radicals. For the ortho OH-toluene bicyclic peroxy radicals, for example, the reaction with NO occurs at oxygen molecules attached to either C4 or C6 on the ring, forming bicyclic alkoxy radicals. Subsequently, the bicyclic alkoxy radical undergoes β-scission to form an acyclic radical,

Scheme 3

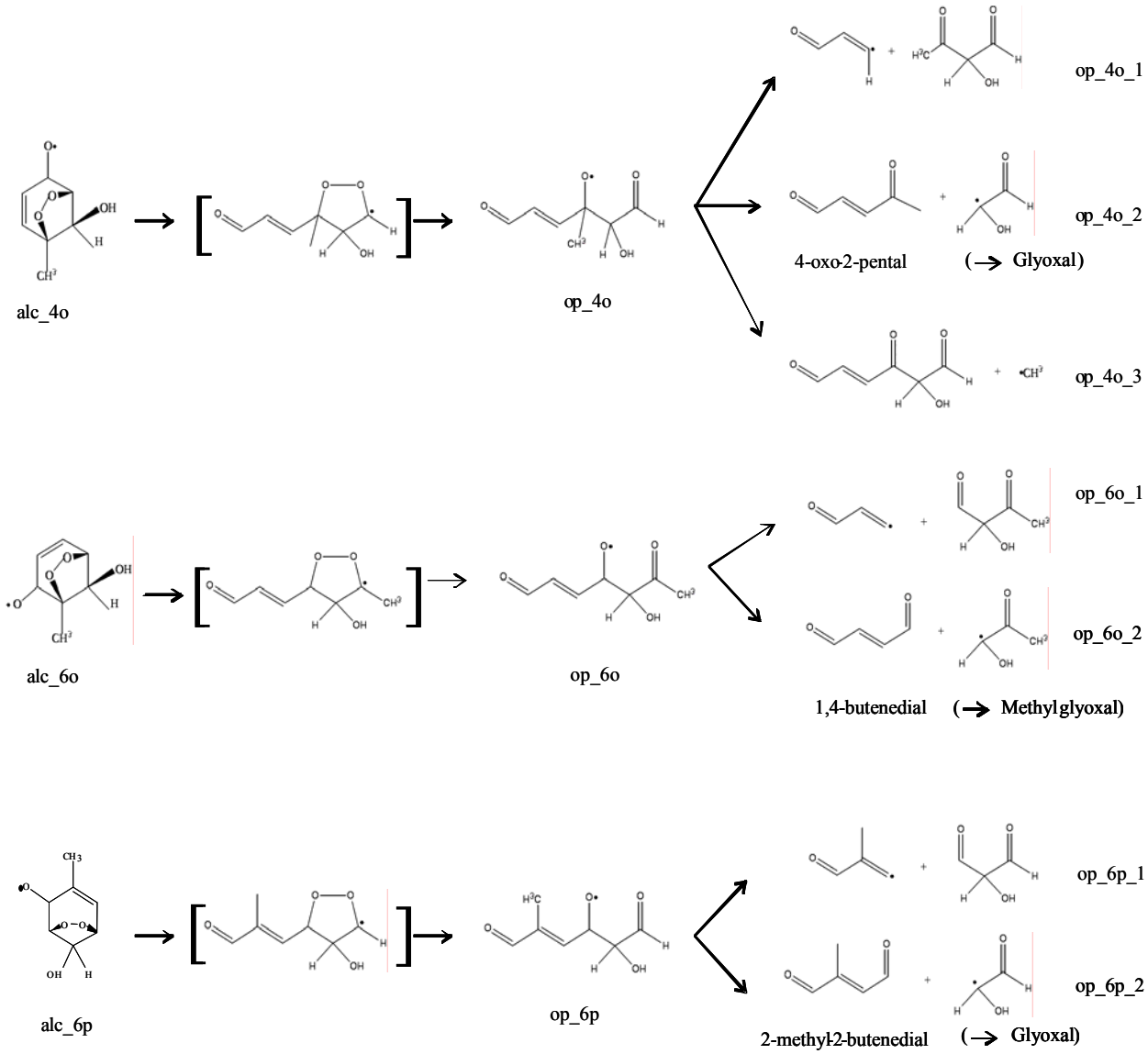
alc_4o
op_4o
op_4o_1
op_4o_2
4-oxo-2-pental
(→ Glyoxal)
op_4o_3
alc_6o
op_6o
op_6o_1
op_6o_2
1,4-butenedial
(→ Methylglyoxal)
alc_6p
op_6p
op_6p_1
op_6p_2
2-methyl-2-butenedial
(→ Glyoxal)

which is followed by unimolecular decomposition pathways to form saturated and unsaturated carbonyl products.

Laboratory studies have been conducted to identify the oxidation products of aromatic hydrocarbons in both the gas and particle phases. Forstner *et al.* [1997] examined aerosol products from several irradiated aromatic hydrocarbon/NO*x* systems including toluene, *m*-, *p*-xylene, ethylbenzene, 1,2,4,-trimethylbenzene, and *m*-, *p*-ethyltoluene. They found a number of aromatic ring-retaining products as well as numerous furan type compounds some of which had been reported as present in the gas phase [*Bierbach et al.*, 1994; *Smith et al.*, 1998]. One of the reported compounds, 3-methyl-2,5-furandione, was found to comprise from 16–61% of the particle phase. Approximately 30% of the total aerosol yield was reportedly identified. Another recent study of the SOA products from toluene photooxidation found a number of ring fragmentation products such as polyketones and hydroxy polyketones in the particle phase [*Edney et al.*, 2001]. Similarly, Jang et al. [2001] detected several aromatic and non-aromatic ring-retaining compounds and a series of saturated and unsaturated ring-opening products in the gas and particle phases from the photooxidation of toluene/propene/NOx mixtures.

Volkamer et al. [2001] reported a 39 ± 10% yield of glyoxal at the EUPHORE outdoor simulation chamber and that ring-cleavage pathways involving the bicycloalkyl radical were major pathways in the oxidation of monocyclic aromatic hydrocarbons. Yu et al. [2001] identified gas-phase carbonyl products from the oxidation of alkylbenzenes including toluene in the presence of nitrogen oxides (NO_x) using GC/MS

detection by O-(2,3,4,5,6-pentafluorobenzyl)-hydroxylamine (PFBHA) derivatives. SOA formation sampled on quartz fiber filters has also been observed in the alkylbenzene-NO_x system [Forstner et al., 1997]. Few theoretical studies have attempted to investigate the ring cleavage reaction from the oxidation of toluene [*Andino et al*., 1996].

In this Chapter, we investigate the formations of the bicyclic alkoxy radicals, their ring cleavages to form the acyclic radicals, and the unimolecular decomposition of acyclic radical to form the saturated and unsaturated carbonyl products. The Density functional theory (DFT) and ab initio methods are employed to obtain the geometries and energies of intermediate radicals and products. The activation barriers for the decomposition pathways were analyzed to assess the energetically favorable pathways for the formation of final products. We also emphasize the relevance of the present theoretical work compared to available experimental product studies.

The theoretical method is similar to those discussed in Chapters 2 and 3.

4.2 Results and Discussions

4.2.1 Formation of Bicyclic Alkoxy Radicals

Geometry optimizations of these bicyclic alkoxy radicals were performed at B3LYP/6-31G(d,p) level of theory, using the geometries of the corresponding bicyclic peroxy radicals [*Suh et al*., 2003], with an oxygen atom removed. For each bicyclic alkoxy radical additional calculations were performed to explore the possible rotational comformers. The evaluation of the vibrational frequencies confirmed that all bicyclic

alkoxy radicals reported here represent minima on the potential energy surface. Figure 4.1 illustrates the equilibrium structures for the bicyclic alkoxy radicals. Comparison of the equilibrium geometries of the alkoxy radicals with those of the bicyclic peroxy radicals that we recently reported shows that the geometries of the bicyclic alkoxy radicals are similar to those of the bicyclic peroxy radicals, with the exception of the C-O radical bond distances. The removal of the oxygen atom from the bicyclic peroxy radicals leads to a shortening of C-O radial bond. The distances for C-O radicals of all alc_4o, alc_6o and alc_6p are 1.37 Å , 0.11 Å shorter than those of the C-O bond of the corresponding bicyclic peroxy radicals. The bond lengths of the bridged O-O and C-O from the hydroxyl group are unchanged. It is noted that intermolecular hydrogen bonding still exists. The hydrogen bonding involves the O and the H atom from the carbon attached the O radical. The hydrogen bond length of Al_O13_4 is 1.96 Á .

4.2.2 Structures and Energies of Acyclic Radicals

For the bicyclic alkoxy radical, β-fragmentation takes place, forming the acyclic radical. Scheme 3 shows the mechanism of the ring fragmentation of the bicyclic alkoxy radicals. For the search of the transition state of the ring fragmentation, the bond between the β-carbon and the carbon attached with the oxygen atom was successively increased. Once an initial geometry optimization reached convergence, a frequency calculation was performed to determine whether this optimized geometry represented a

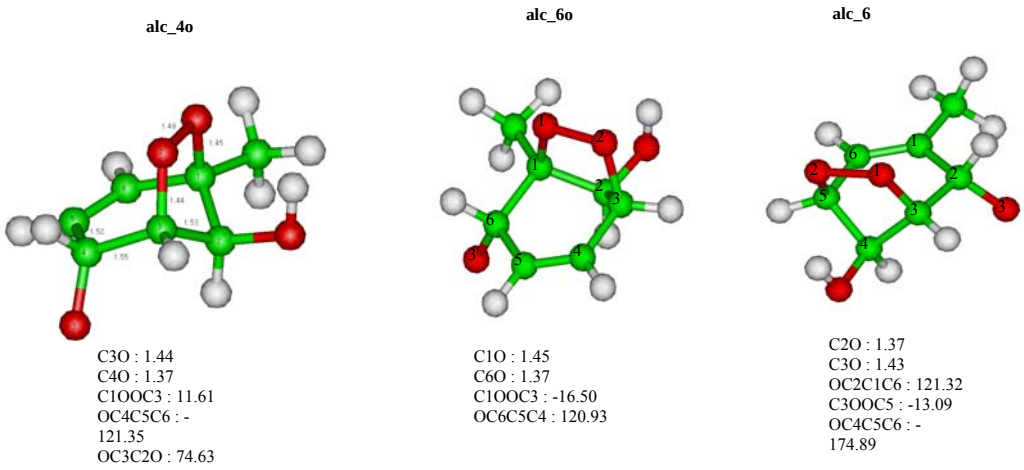

Figure 4.1. Structures of bicyclic alkoxy radicals at the B3LYP/6-31G(d,p) level of theory.

first-order saddle point. One imaginary component in the calculated vibrational frequencies identified a transition state. The motions pertinent to the β fragmentation are clearly present, whereas there is little evidence of O-O bond cleavage that take place beyond the transition state. Figure 4.2 depicts the optimized geometries of the transition states. The distances of the transition states for the ring opening of the bicyclic alkoxy radicals alc_4o, alc_6o, and alc_6p are 2.16, 2.1 and 2.13 Å, respectively. The energy barriers for the cleavage of the C-C bonds of the alc_4o, alc_6o, and alc_6p are 7.3, 4.2, and 7.5 kcal mol^{-1}, respectively. Spin contamination in the TS calculations is nonnegligible, but is effectively removed after spin projection.

We considered a substantial amount of possible spatial orientations for the bridged O-O bond attached above the ring and the carbon chain with one localized double bond on the ring in the bicyclic alkoxy radical to obtain the global minima of the equilibrium structures of acyclic radicals. The torsion angles of the C-C-C-C and C-O-O-C, along with the relative orientations of the cis- and trans- formations of the carbon chain were considered. There are convincing indications from our calculations that the partially open chain intermediate shown in the brackets of scheme 3 does not exist. On attempting to define its structure as an energy minimum, the O-O bond spontaneously cleaves. Figure 4.3 depicts the optimized geometries of the lowest energy conformations of the acyclic radicals op_4o, op_6o, and op_6p. It is interesting that a planar O-C-C-C center which has the delocalized allyl-π system reveals a stable structure formation in the acyclic radicals. Another interesting feature is that the ring

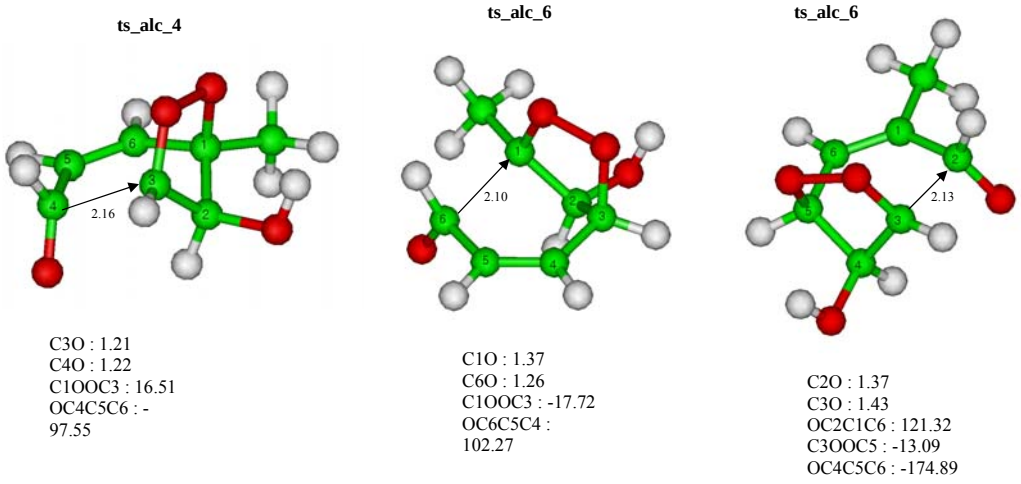

Figure 4.2. Optimized geometries of the transition states of the bicyclic alkoxy radicals at the B3LYP/6-31G(d,p) level of theory.

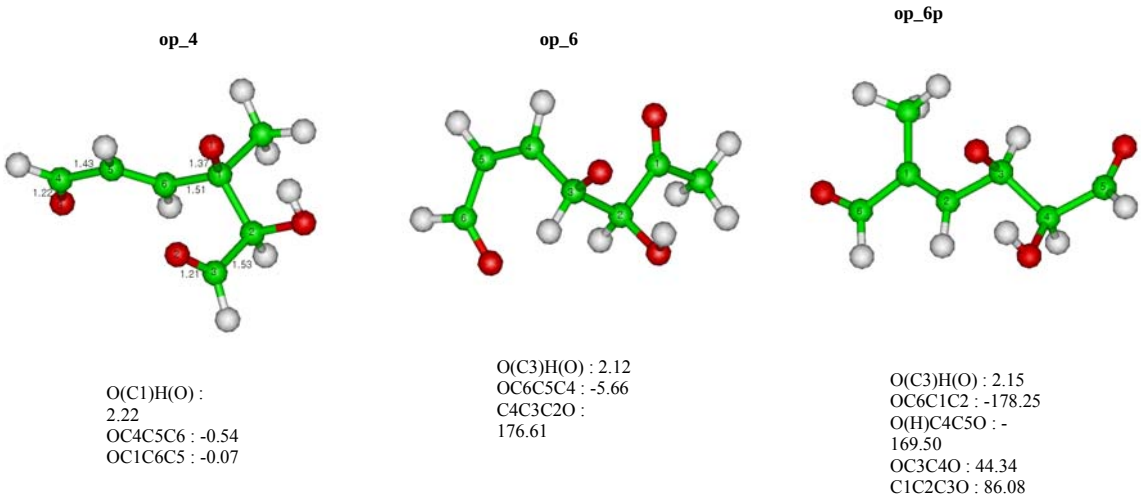

Figure 4.3. Structures of acyclic radicals at the B3LYP/6-31G(d,p) level of theory.

cleavage of the five- member ring of O-O-C-C-C radical results in the one localized C-O bond and the intramolecular hydrogen bonding in the acyclic radical. For example, the hydrogen bonding in op_4O involves the O atom attached at C1 and the H atom from the hydroxy group. The length of the hydrogen bonding of acyclic radicals ranges from 2.12 to 2.22 Å. The relatively longer length involves a five-member ring. The acyclic radical op_6O has another intramolecular hydrogen bonding which involves the terminal O atom from the carbon chain and the H atom attached at C3. It explains that the reaction energy of the acyclic radical op_6O is more stable by 7 and 5.5 kcal mol^{-1} than those of op_4O and op_6P, respectively.

The zero-point corrected reaction energies for the formation of acyclic radicals and their activation energies are listed in Table 4.1 and Table 4.2, respectively. Spin contamination for the acyclic radicals are minimal. The reaction energies of acyclic radicals op_4O and op_6O are 47.79 and 55.18 kcal mol^{-1}, significantly more stable than those of acl_4o and alc_6o, respectively. The reaction energy of op_6P is also 49.5 kcal mol^{-1} more stable than that of alc_6p.

4.2.3 Decomposition of Acyclic Radicals

The decomposition pathways of the C-C bond of the three acyclic radicals were studied according to the energetics of their transition states and products to access the corresponding relative feasibilities (scheme 3). Transition state search for the C-C bond cleavage of the acyclic radical was performed by using TS keyword in geometry optimization at the B3LYP/6-31G(d,p) level of theory. The relevant transition state

structures of acyclic radicals are shown in Figure 4.4. Arrows in this figure display the vibrational modes along the reaction coordinates.

The C-C bond scission of the acyclic radical occurs adjacent to the O radical center. For example, three possible decomposition pathways for acyclic radical op_4O are considered. The other C-C bond next to the O radical center is strengthened as a result of the electron density shift from fragmentation between the carbon attached to the oxygen atom and the saturated carbon. The lengths of the transition states for the C-C cleavage are in the ranges of 2.01- 2.1 Å.

On the basis of the B3LYP/6-31(d,p) optimized geometries, single point energy calculation at MP2 and CCSD(T) level were performed to calculate the activation and reaction energies of the C-C bond decomposition pathways of the acyclic radicals. The calculated activation energies and reaction energies are listed in Table 4.1 and 4.2, respectively. Table 4.1 indicates that the calculated reaction energies depend on the electron correlation and basis set. The calculated activation energies are found to be sensitive to electron correlation and basis set effect. The activation energies calculated with CCSD(T)/6-31 G(d) are higher that those obtained with B3LYP/6-31G(d,p), with the difference ranging from 2.0 to 4.8 kcal mol^{-1}. The basis set correction factors are in the range of -0.9 to -3.6 kcal mol^{-1}.

Our calculated activation barriers via decomposition were analyzed to assess the energetically favorable pathways. Table 4.2 indicates that the decomposition pathways at the CCSD(T)/6-31G(d) + CF level of theory proceed with relatively large activation barriers, ranging from 2.4 to 29.9 kcal mol^{-1}. The reactions op_4o_1, op_4o_3, and

Table 4.1. Reaction energies (kcal mol^{-1}) for decomposition of opened carbonyl compounds with zero-point energy included.[a]

Reaction	B3LYP/6-31G(d,p)	CCSD(T)/ 6-31G(d)	CCSD(T)/ 6-31G(d)+CF
op_4o_1	9.4	16.96	13.41
op_4o_2	-26.3	-14.97	-16.79
op_4o_3	0.6	5.3	2.4
op_6o_1	17.5	23.4	20.1
op_6o_2	-17.6	-8.7	-11.1
op_6p_1	17.2	24.1	20.8
op_6p_2	-21.0	-11.7	-14

[a] Using the CCSD(T)/6-31G(d) + CF//B3LYP/6-31G(d,p) energies.

Table 4.2. Activation energies (kcal mol^{-1}) for decomposition of acyclic radicals with zero-point energy included.

Reaction	B3LYP/6-31G(d,p)	CCSD(T)/ 6-31G(d)	CCSD(T)/ 6-31G(d)+CF
op_4o_1	23.67	28.82	25.85
op_4o_2	-2.06	3.36	2.43
op_4o_3	9.2	16.44	14.02
op_6o_1	26.75	32.6	29.9
op_6o_2	2	5.01	3.94
op_6p_1	20.3	27.1	24.6
op_6p_2	2.4	7.0	5.6

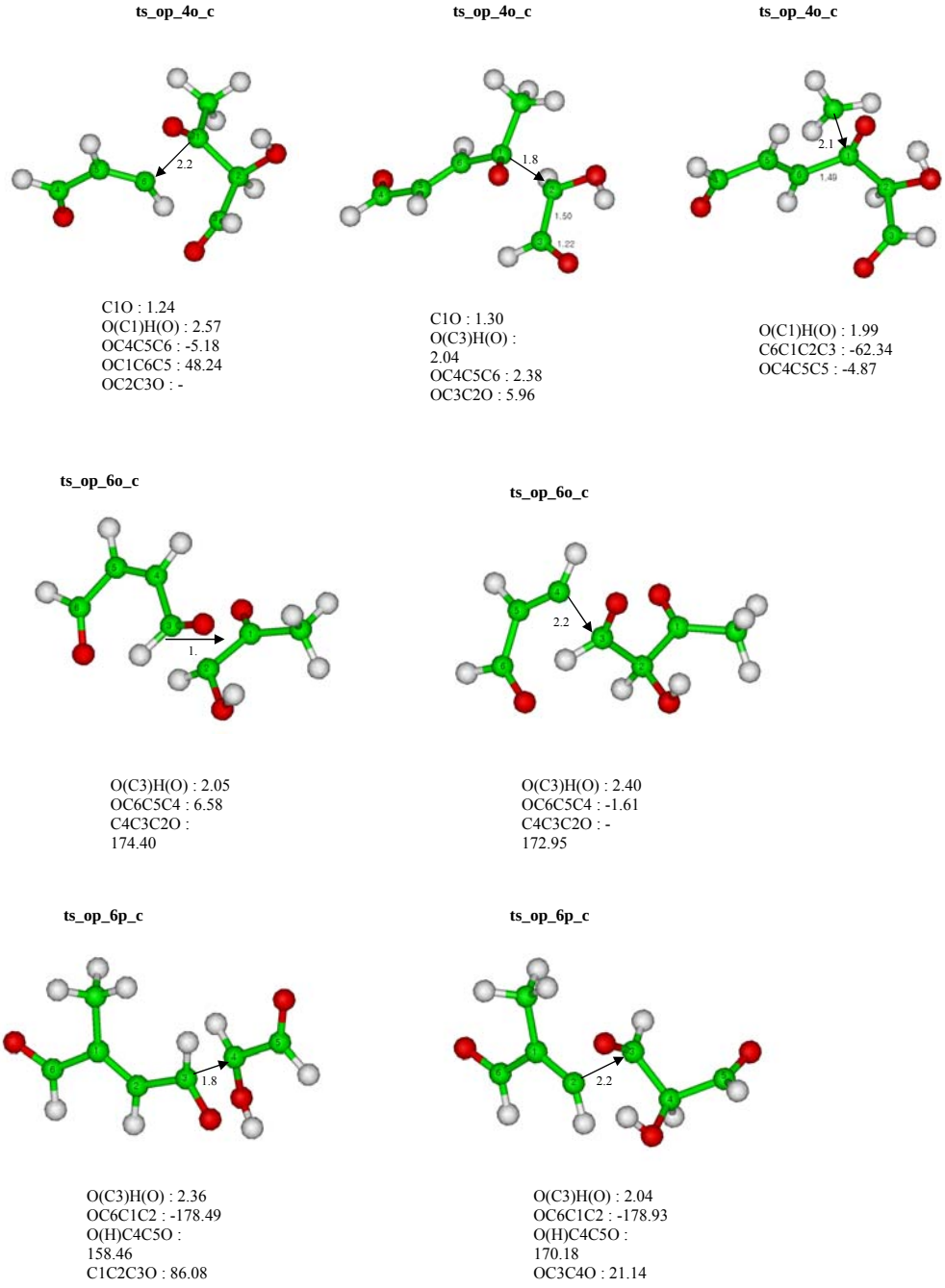

Figure 4.4 . Optimized geometries of the transition states of C-C- bond cleavage at the B3LYP/6-31G(d,p) level of theory.

op_6p_1 are endothermic, with the reaction energies in the range of 2.4 to 20.8 kcal mol^{-1}. For op_4o radical the pathway op_4o_2 leading to glyoxal is exothermic, with the lowest activation barrier of 2.4 kcal mol^{-1}. For op_6o radical, the preferable pathway is op_6o_2 to form methyl glyoxal and 1,4-butanedial with an activation barrier of 3.94 kcal mol^{-1}. For op_6p radical, op_6p_2 corresponds to the preferable pathway leading to the formation of glyoxal with an activation barrier of 5.6 kcal mol^{-1}. Potential energy surface diagrams involving the C-C bond dissociation pathways of the bicyclic alkoxy radicals are shown in Figure 4.5 calculated at B3LYP/6-31G(d,p).

The calculated high-pressure limit rate constants for acyclic radical decomposition and the corresponding recombination at 300 K are listed in Table 4.3. C-C bond dissociation for the reactions op_4o_2, op_6o_2, and op_6p_2 occurs with the rate constants of $1.1x10^{11}$, $3.1x10^{11}$, and $2.2x10^{9}$ s^{-1}, respectively, whereas the rates for the others are significantly smaller. Table 4.3 also indicates that the bimolecular recombination rates to reform the acyclic radicals are very slow. For acyclic radicals op_4o, op_6o,and op_6p, the C-C bond cleavage to lose the $\cdot CH_2O(CH_3)COH$ radicals are the dominant dissociation pathways. This occurs because the unsaturated carbonyl compounds have a stabilizing effect in terms of the central C_{sp2} - C_{sp2} bond and by the overlap of p-orbitals to give Л-bonding. A previous theoretical work by Andino et al [1996] reported the calculation of the ΔH_{rxn} for the decomposition of the acyclic radical, using the NIST Structures and Properties estimation program based on the group activity theory. Group activity calculations indicated that fragmentation between

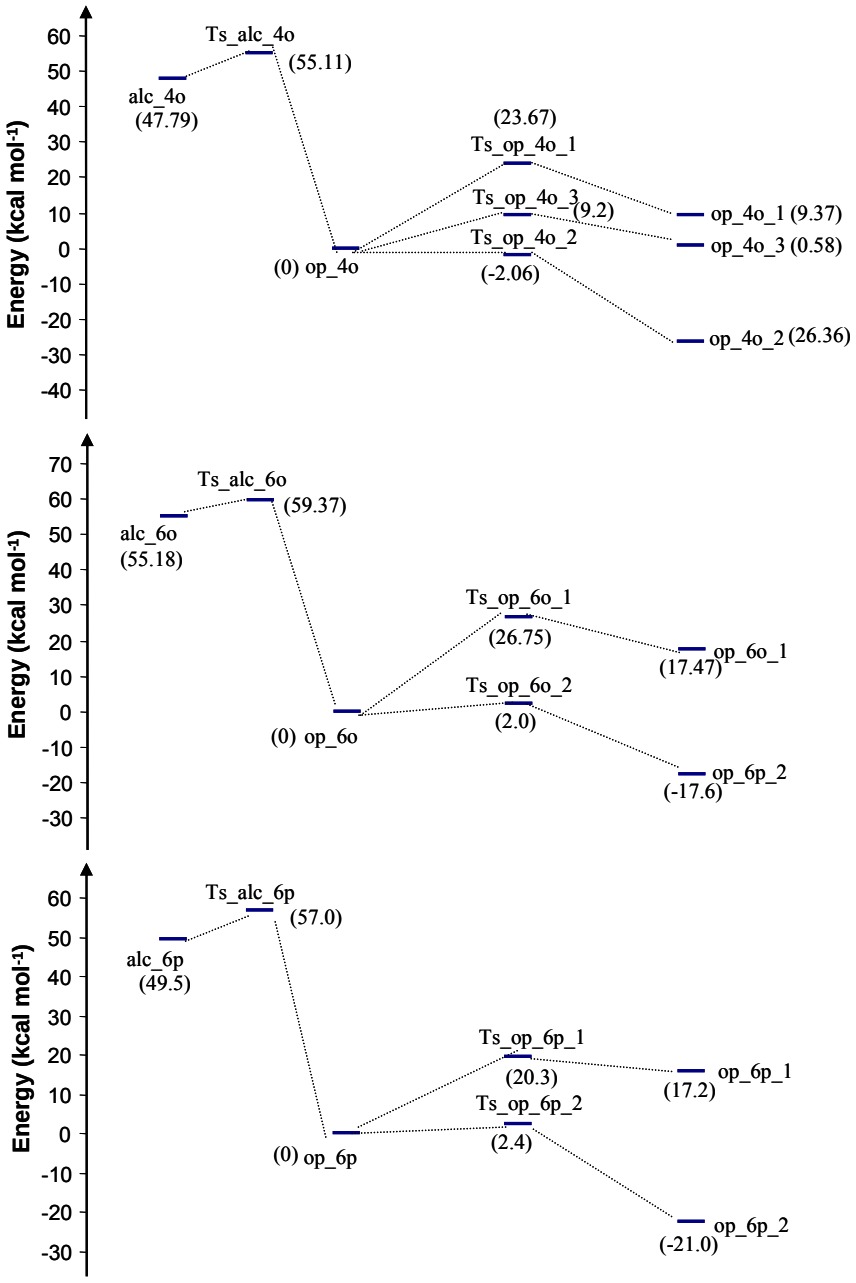

Figure 4.5. Potential energy surface (PES) involving the dissociation of the bicyclc alkoxy radicals obtained by using B3LYP/6-31G(d,p).

Table 4.3. Unimolecular rate constants, recombination rate constants, and equilibrium constants of acyclic radical decomposition reactions at 300K.

Reaction	k_{uni} (s^{-1})	k_{rec} (cm^3 $molecule^{-1}$ s^{-1})	K_{eq} (molecule cm^{-3})
op_4o_1	$1.5x10^{-5}$	$7.0x10^{-44}$	$2.4x10^{35}$
op_4o_2	$2.0x10^{14}$	$5.7x10^{4}$	$3.5x10^{9}$
op_4o_3	$9.9x10^{2}$	$5.4x10^{-27}$	$8.7x10^{27}$
op_6o_1	$5.7x10^{-10}$	$7.6x10^{-24}$	$1.7x10^{41}$
op_6o_2	$3.1x10^{10}$	$3.1x10^{-12}$	$3.4x10^{15}$
op_6p_1	$8.0x10^{-6}$	$8.8x10^{-47}$	$2.2x10^{40}$
op_6p_2	$2.2x10^{9}$	$4.2x10^{-9}$	$5.3x10^{17}$

the carbon with the O atom attached to it and the unsaturated carbon center is the favored path.

4.2.4 Atmospheric Implications

In scheme 4, the reactions in the box represent the favorable decomposition pathway of the bicyclic alkoxy radical after discarding the other possible reaction routes, which involve high activation barriers. Ring-opening products are glyoxal, methyl glyoxal, and unsaturated dicarbonyl compounds having carbon numbers between four and seven [*Yu et al.*, 1997]. These dicarbonyl compounds have been found to be highly reactive and have been found to be removed by photolysis as well as reaction by OH or ozone [*Bierbach et al.*, 1994]. Alternatively, these dicarbonyl compounds result in the formation of dihydro-2,5,-furandione, 2,5-furandione, and 3-methyl-2,5-furandione which have been identified as the primary SOA components [*Seinfeld et al*., 1997; *Odum et al*., 1997; *Forstner et al*., 1997]. Dicarbonly compounds such as 1,4-butenedial and 4-oxo-pentenal have been identified as primary products [*Volkamer et al.*, 2001]. Smith *et al*. [1998] reported that the yield of glyoxal and methylglyoxal from the reaction of toluene with OH was about 14%. Recently, Volkamer et al. [2001] have shown that one of the principal oxidation product, glyoxal,

is a primary product that gave a yield of (39.0 ± 10.2)%. In the troposphere, toluene is removed by reaction with OH primarily through a ring-addition mechanism. This process leads mainly to the formation of ring-opening products but also to the formation of cresols. On the basis of results from Chapter II, III and ~18% yield of cresol formation [*Smith et al.*, 1998], we estimated the yields for glyoxal formation at about 50% and methyl glyoxal formation at about 11%.

Several ring-retaining compounds in the gas and particle phases from the photooxidation of toluene/propene/NO_x mixtures have been detected as primary products [*Jang et al.*, 2001; *Forster et al.*, 1997]. However those aromatic ring-retaining products are unlikely to be of importance under atmospheric conditions, because the initial concentrations from their studies were in the level of ppm for toluene and NO_x, which allow more reaction of the OH-toluene adduct with NO_2 occurs than that with O_2.

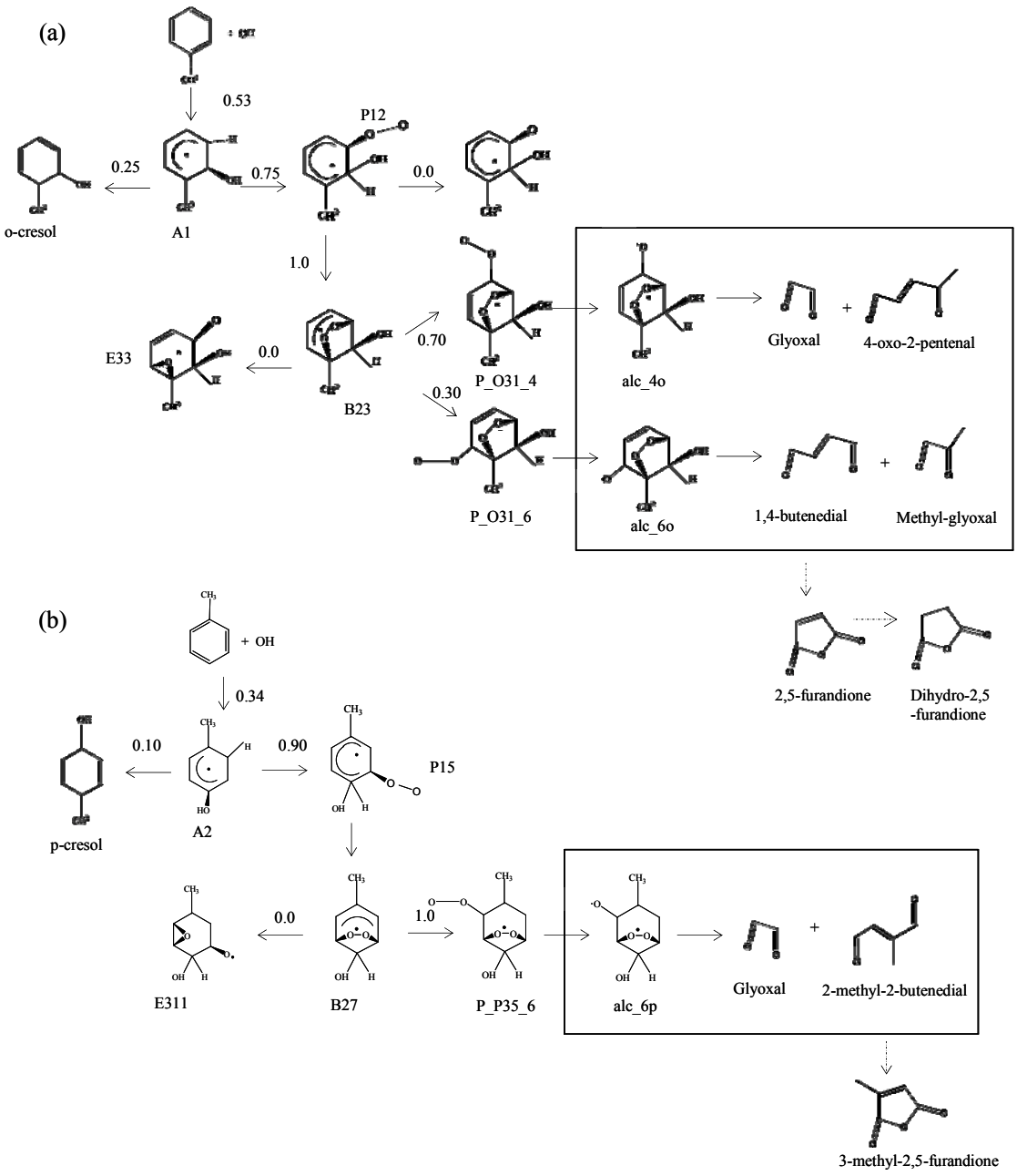
(a)
0.53
P12
0.25
0.75
0.0
o-cresol
A1
1.0
E33
0.0
0.70
B23
P_O31_4
0.30
P_O31_6
alc_4o
alc_6o
Glyoxal
4-oxo-2-pentenal
1,4-butenedial
Methyl-glyoxal
2,5-furandione
Dihydro-2,5
-furandione
(b)
+ OH
0.34
0.10
0.90
P15
p-cresol
A2
0.0
1.0
E311
B27
P_P35_6
alc_6p
Glyoxal
2-methyl-2-butenedial
3-methyl-2,5-furandione

Scheme 4

4.3 Summary and Conclusions

We have presented DFT and ab initio molecular orbital calculations of the bicyclic alkoxy radicals from the toluene reaction initiated by OH and their decomposition pathways. The geometries and energetics of the three isomers of the bicyclic alkoxy radicals and the transition states and products of their decomposition reactions have been investigated. In addition, we have calculated the high-pressure limit rate constants of the C-C bond dissociation of the acyclic radicals, using the presently obtained activation energies and transition state theory (TST). The activation energy barriers of decomposition of the acyclic radicals are in the range of 2 to 30 kcal mol^{-1}, and the calculated dissociation rates for the acyclic radicals are in the range of $6x10^{-10}$ to $2x10^{14}$ s^{-1}. The results suggest that fast decomposition rates of acyclic radicals provide significant glyoxal formation and dicarbonyl compounds such as 1,4-butenedial and 2-methyl-2-butenedial. These dicarbonyl compounds result in the formation of dihydro-2,5,-furandione, 2,5-furandione, and 3-methyl-2,5-furandione which are the primary SOA components.

CHAPTER V

ATMOSPHERIC NEW PARTICLE FORMATION ENHANCED BY ORGANIC ACIDS*

Atmospheric aerosols often contain a substantial fraction of organic matter, but the role of organic compounds in new nanometer-sized particle formation is highly uncertain. Laboratory experiments show that nucleation of sulfuric acid is considerably enhanced in the presence of aromatic acids. Theoretical calculations identify the formation of an unusually stable aromatic acid–sulfuric acid complex, which likely leads to a reduced nucleation barrier. The results imply that the interaction between organic and sulfuric acids promotes efficient formation of organic and sulfate aerosols in the polluted atmosphere because of emissions from burning of fossil fuels, which strongly affect human health and global climate.

5.1 Introduction

Aerosols influence the Earth-atmosphere system in several distinct ways [*Finlayson-Pitts and Pitts*, 2000; *Seinfeld and Pandis*, 1998]. Concerns over the human

* Reprinted with permission from "Atmospheric New Particle Formation Enhanced by Organic Acids" by Zhang, R. Y., I. Suh, J. Zhao, D. Zhang, E. C. Fortner, X. Tie, L. T. Molina, and M. J. Molina, 2004, Science, 304, 1487-1490. (Available at http://www.sciencemag.org/)

health effects of fine particulate matter constitute the most important element in formulating the national ambient air quality standard [*EPA*, 1996]. Also, aerosols directly or indirectly affect the Earth's radiation budget [*Charlson et al*., 1987; *Houghton*, 2001], and light absorption by aerosols causes visibility degradation. Furthermore, modification of clouds and precipitation by aerosols may enhance lightning activity and thus influence tropospheric chemistry [*Orville et al*., 2001; *Zhang et al*., 2003]. The impacts of particulate matter on health, radiation, and cloud microphysics are strongly dependent on the particle sizes.

Several processes determine the aerosol size distribution, including new particle production (as a result of gas-to-particle conversion), growth due to condensation and coagulation, removal rates, and primary emissions. New particle formation or nucleation is the least understood of these steps [*Kulmala*., 2003]. Much of the previous research has focused on nucleation of sulfuric acid, because sulfate represents an important component of the nucleation mode aerosol [*Stray et al.*, 1994; *Laskin et al*., 2003]. It is commonly recognized that binary nucleation of H_2O-H_2SO_4 is not efficient enough to explain atmospheric new particle formation [*Boy et al*., 2003]. Progress recently has been made in assessing the importance of ternary water–sulfuric acid–ammonia nucleation [*Weber et al*., 1999; *Ball et al*., 1999], ion-induced nucleation [*Yu et al*., 2001; *Lee et al*., 2003], and nucleation involving iodine species [*O'Dowd et al*., 2002; *Klob et al*., 2002].

The role of organic compounds in new particle formation is another potentially important issue [*Martin et al*., 1997]. Atmospheric measurements reveal that aerosols

often contain a considerable amount of organic matter [*Chebbi and Carlier*, 1996; *Kavouras et al.*, 1998; *O'Dowd et al*., 2002; *Gasparini et al*., 2004]. During photooxidation of volatile organic compounds (VOCs), non- or semivolatile organic products are produced that contribute to secondary organic aerosol (SOA) formation. For example, in the urban atmosphere the aromatic component in gasoline (mainly toluene and xylenes) is responsible for SOA formation caused by oxidation of these compounds [*Odum et al*., 1997]. Current theory of SOA formation assumes that condensation of low-volatility organic species such as carboxylic or dicarboxylic acids occurs on preexisting particles from primary emissions or formed by homogeneous nucleation, most probably involving sulfuric acid–ammonia–water or ions [*Kulmala*, 2003]. Alternatively, it is suggested that SOA nucleation may occur through the formation of stable organic heterodimers [*Hoffmann et al*., 1998]. Currently, few experimental studies have investigated new particle formation from organic acids. Another process, which also influences the chemical composition of organic aerosols, involves adsorption of gaseous species onto particulate matter. On the basis of consideration of the thermodynamic equilibrium distribution of a compound between the gas and condensed phases, a gas-particle partitioning model has been proposed [*Pankow et al*., 1994b] and invoked to explain the observed correlation between the SOA yield and the organic aerosol mass concentration [*Odum et al*., 1997; *Odum et al*., 1996]. More recently, it has been suggested that sulfate aerosols catalyze heterogeneous reactions of carbonyl compounds, leading to a considerably enhanced SOA yield [*Jang*

et al., 2002]. The growth of SOA from both mechanisms depends on preexisting particles, which are linked to new particle formation or primary emissions.

5.2 Experimental

To assess the role of low-volatility organic species in new particle formation, we performed laboratory studies of particle nucleation from aromatic acid vapors and their mixtures with H_2SO_4. The schematic diagram for the experimental setup is shown in Figure 5.1. Each of the experimental components was controlled by National Instruments Labview software with data acquisition cards.

The aerosol chamber made of a jacketed glass tube of 2.45 cm i.d. and 60 cm in length was employed to generate the nano-scale particles. The inlets of the samples were heated to prevent condensing the materials on the wall. The average flow speed inside of the chamber was 7.2 cm/s. A filter capsule was connected from the N_2 gas tank to remove possible contaminated materials. The chamber was rinsed with deionized water when switched to H_2SO_4/H_2O/organic acid from H_2SO_4/H_2O. The H_2SO_4 vapor was introduced by flowing N_2 carrier gas through the bubbler containing 10 ml of 98% H_2SO_4 solution. The temperature of the H_2SO_4 source was regulated by a heating bath in the range of 30~37^oC. The line of flowing H_2SO_4/N_2 was heated by the heating tape to prevent condensation. H_2O vapor was added by flowing the N_2 carrier gas through the bubbler at room temperature. The inlets (1/4 inch in ID) of H_2SO_4/N_2 and H_2O/N_2 were positioned *horizontally* and the gases were mixed within 5cm of the beginning of the chamber.

Calibrations of H_2SO_4 and the organic acids were performed by ID-CIMS or PTR-MS. The PTR-MS and CIMS methods have been described in previous studies [Fortner et al., 2004; *Zhao et al*., 2004]. Briefly, H_2SO_4 was detected as a negative ion after undergoing specific ion-molecule reaction. The chemical ionization was initiated by

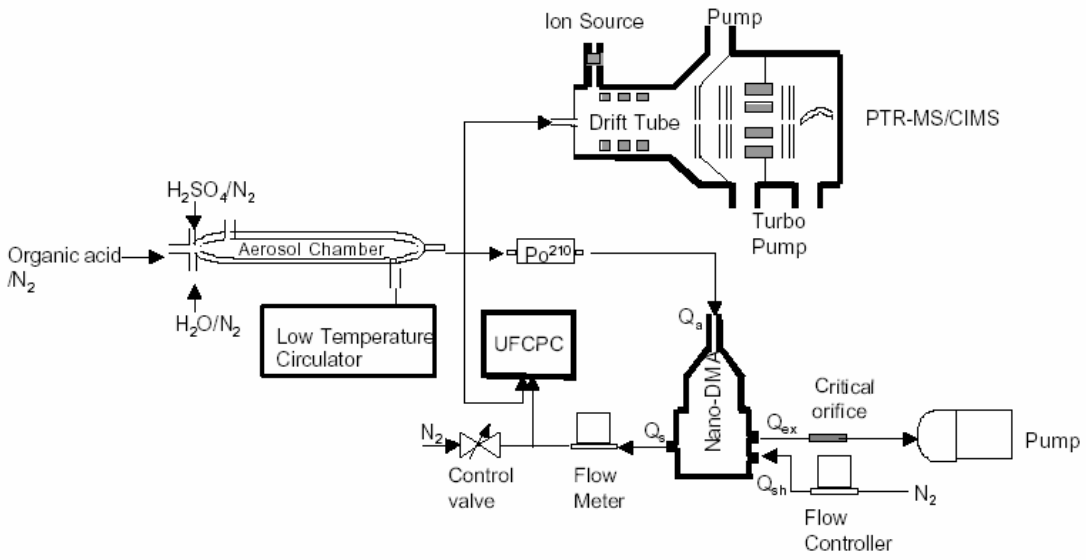

Figure 5.1. Schematic representation of the experimental setup.

injecting SF_6^- at the downstream end of the drift tube. The following reaction was used to detect H_2SO_4 :

$$H_2SO_4 + SF_6^- \rightarrow HSO_4^- + SF_6(H)$$

The measured concentration of H_2SO_4 is about 2 orders of magnitude lower than the concentration calculated by the flow ratios. The organic acids were detected as positive ions after the proton transfer reaction :

$$R + H_3O^+ \rightarrow RH^+ + H_2O$$

The protonated product ions RH^+ were detected by mass spectrometry.

Aromatic acids, such as benzoic ($C_7H_6O_2$), *p*-toluic ($C_8H_8O_2$), and *m*-toluic ($C_8H_8O_2$) acids, are products from photochemical degradation of aromatic hydrocarbons emitted from automobiles in the urban atmosphere [*Suh et al*., 2003] and have been identified in the particle phase [*Forstner et al*., 1997; *Jang et al*., 2001]. Nanometer-sized particles were produced in an aerosol chamber, and the particle concentration and size distribution were monitored with a nanodifferential mobility analyzer (model 3085, TSI Incorporated Particle Instruments) and an ultrafine particle counter (model 3025A, TSI Incorporated Particle Instruments, St. Paul, MN) capable of measuring particle sizes as small as 3 nm (>50% detection). The sampled particle flow, 1.0 L/min, was brought to a Boltzmann charge equilibrium by passing the particles through a Polonium 210 radioactive source and then injecting them into the nano-DMA with a 10.0 L/min flow of particle free sheath flow. Po^{210} bipolar charge was less efficient than the unipolar charger because the presence of both positive and negative ions tends to neutralize the aerosol charge. This charger yielded fewer charged nanoparticles for

analysis [*Herberti et al*., 2001]. The high voltage electric fields created by the ultravolt high voltage power supply drew the positively charged particles toward the axis of the nano-DMA. Particles within a certain mobility range exited an aperture and were counted by a UFCPC. A short path length and high inlet flow in the nano-DMA shortened the particle residence time, which reduced diffusional losses of nanometer size particles. Upon scanning the voltage from 0 to 0.13V, the distribution of particles was measured in the range of 3 to 13 nm particle diameters. The nucleation time was estimated to be in the range of 7 to 12 s. For the nucleation experiments involving sulfuric acid and organic/sulfuric acid mixtures, the experiments were performed at 298 ±2 K. For experiments involving homomolecular nucleation of organic acids, the temperature was regulated between 220 and 298 K. All experiments were performed at a pressure of one atm.

5.3 Results and Discussions

5.3.1 Particle Measurement

H_2SO_4 aerosols were generated by interaction between gas-phase H_2SO_4 and H_2O vapor. The slowly varied temperature of the H_2SO_4 reservoir resulted in a gaseous H_2SO_4 concentration in the range of 10^9 to 10^{10} molecule cm^{-3}. Shown in Figure 5.2 are nanometer size particles formed in the range of 3 to 10 nm for the H_2SO_4-H_2O system. The observed particle concentration increased when the gaseous H_2SO_4 concentration was increased from 5.8×10^9 and 8.2×10^9 molecule cm^{-3} in Figure 5.2(a). A significant increase in the number of particles occurred in the presence of 0.04 ppb benzoic acid by

a factor of 5 in Figure 5.2(a). In Figure 5.2(b), the concentration of H_2SO_4 was fixed at $7.5x10^9$ molecule cm^{-3}, and the concentration of benzoic acid vapor increased from 0.03 ppb to 0.05 ppb. The higher amounts of benzoic acid resulted in more pronounced particle formation. Figure 5.2 shows that the measured peak diameter of the particle distribution shifted slightly to a larger size with addition of benzoic acid, implying that the presence of benzoic acid both enhanced nucleation and contributed to the growth of the newly nucleated particles. Substantially larger peak diameters (>10 nm) were detected when benzoic acid concentrations were increased by one to two orders of magnitude.

The effect of the organic acid on the particle production was investigated when the aerosol chamber was connected directly to UFCPC. The results for ~5% relative humidity are shown in Figure 5.3. Three organic acids (benzoic acid, m-, and – p- toluic acids) were added in the presence of the H_2O-H_2SO_4 system. The solid triangles were the measured nucleation rates of the H_2O-H_2SO_4 system, and the solid circles obtained in the presence of organic acids show that the nucleation rate was considerably increased The aerosol nucleation rate, *J*, deduced from the measured particle concentration to the nucleation time. In Figure 5.3(a), the significant effect of 0.1 ppb benzoic acid on the nucleation rate is shown. The nucleation rate in the presence of benzoic acid is about a factor of 8 to 10 faster than that of the H_2O-H_2SO_4 binary system. Enhanced nucleation rates were also observed for *p*-toluic and *m*-toluic acids in Figure 5.3(b) and 5.3(c). The nucleation rate was increased by a factor of 5 to 13 in the presence of 0.2 to 0.3 ppb of these two acids.

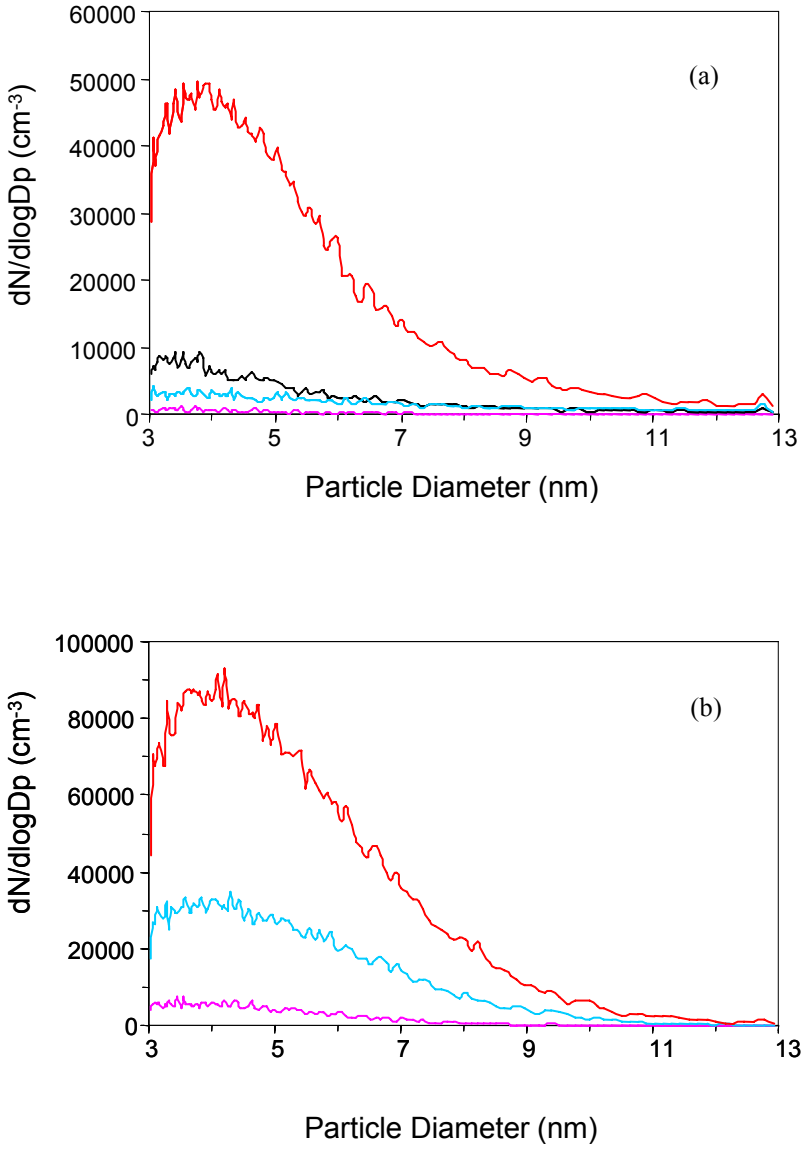

Figure 5.2. (a) Size distributions for sulfate aerosol. Pink and black lines are sulfuric acid aerosol particles with the concentration of 5.8×10^9 and 8.2×10^9 molecule cm^{-3}, respectively, and sky blue and red lines are those in the presence of 0.048 ppb of benzoic acid. (b) Pink line is sulfuric acid aerosol particles with the concentration of 7.5×10^9 molecule cm^{-3} and sky blue and red lines are those in the presence of 0.028 and 0.049 ppb of benzoic acid, respectively.

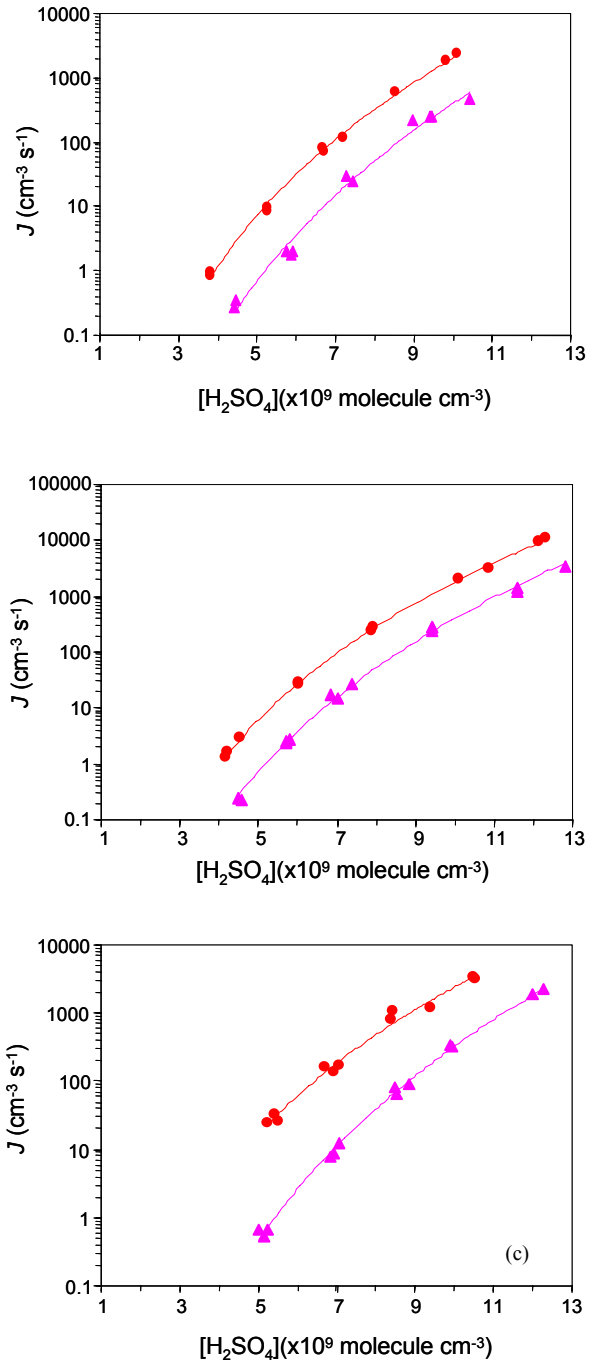

Figure 5.3. Estimated nucleation rate (J) as a function of gaseous H_2SO_4 concentration. The solid triangles correspond to H_2SO_4 aerosol formation with a RH of 5%, and the solid circles correspond to particle formation with 5% RH and in the presence of 0.1 ppb benzoic acid (**A**), 0.2 ppb *p*-toluic acid (**B**), or 0.3 ppb *m*-toluic acid (**C**). The curves are fit to the experimental data. The experiments were performed at 298 ± 2 K and a total pressure of 760 torr.

The nucleation rate is more precisely defined as the rate at which particles of critical size are produced. In this study, we detect only particles larger than 3 nm, and hence the value estimated from the rate of observed particle formation may be smaller than that of cluster formation. In the absence of organic acids, the nucleation rate is dependent on the gas-phase H_2SO_4 concentration and RH. Our measured nucleation rate of the H_2O-H_2SO_4 binary system is qualitatively in agreement with previous experimental studies [*Ball et al*., 1999].

5.3.2 The Effect of Relative Humidity on Particle Formation

The solid triangles shown in Figure 5.4 represent the nucleation rates of the H_2O-H_2SO_4 binary system in 9.5% RH. In comparison with the nucleation rates of the H_2O-H_2SO_4 system at 4.5% RH in Figure 5.3(a), the data suggest that the faster nucleation occurred with the higher relative humidity. This result implies that fewer H_2SO_4 molecules are required to form the nucleus when more H_2O molecules are available. For RH in the range of 4 to 15%, addition of sub-ppb levels of the organic acids consistently led to a larger nucleation rate by a factor of 5 or higher than that of the H_2O-H_2SO_4 binary system.

Small amount of NH_3, 0.17 ppb, are able to promote large enhancements in the rate of particle nucleation in the presence of H_2SO_4- H_2O system [*Ball et al.*, 1999]. Figure 5.5 suggests that the magnitude of the effect of benzoic acid on H_2SO_4 nucleation enhancement appears to be comparable to that for ammonia at similar H_2SO_4 concentration at ~5% RH. The concentration of benzoic acid was 0.04 ppb.

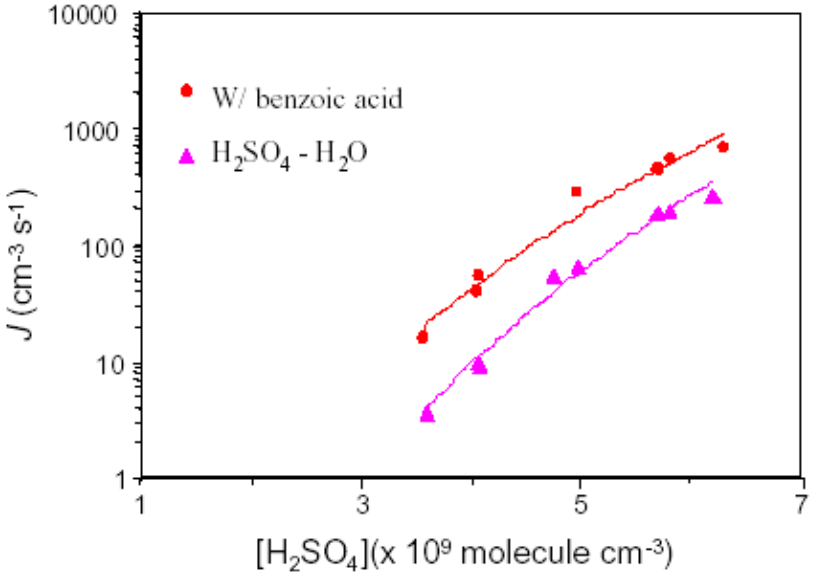

Figure 5.4. Nucleation rates in the $H_2SO_4/H_2O/C_7H_6O_2$ system at 9.5% RH. The concentration of the benzoic acid is 0.04 ppb.

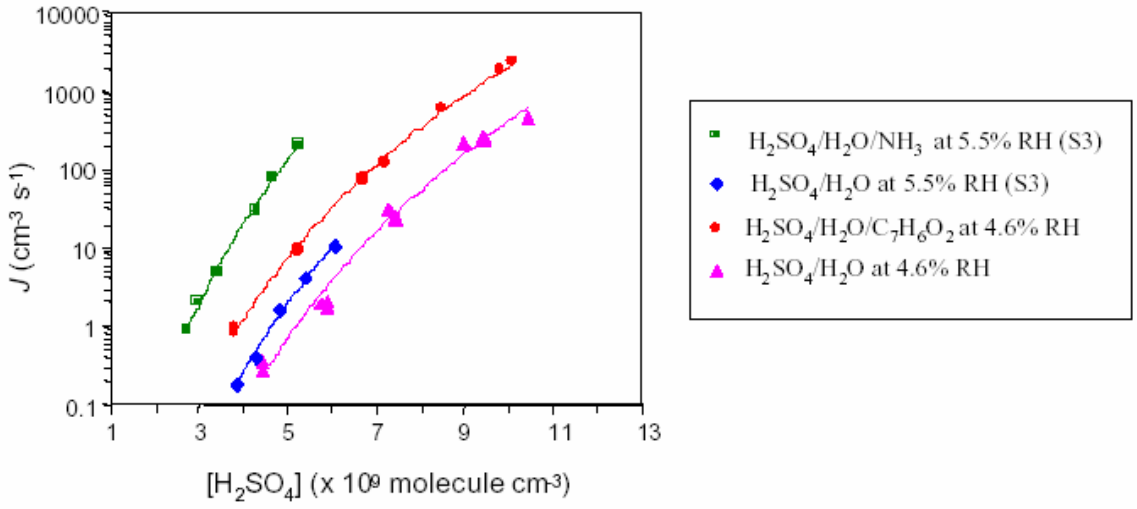

Figure 5.5. Nucleation rates in the $H_2SO_4/H_2O/C_7H_6O_2$ system at 4.6% RH are compared with nucleation rates in the $H_2SO_4/H_2O/NH_3$ system at 5.5% RH presented by Ball et al.

The partial pressures of the organic acids in those experiments were several orders of magnitude smaller than their corresponding equilibrium vapor pressures; that is, the saturation ratio, S , was much smaller than unity. S is defined as the ratio of the partial pressure of the organic acid to its equilibrium vapor pressure at a given temperature. For example, the equilibrium vapor pressures are 7.0×10^{-3} torr for benzoic acid and 1.9×10^{-3} torr for *p*-toluic acid at 298 K, corresponding to saturation mixing ratios of 9.2 and 2.5 ppm (parts per million) at 1 atm, respectively. Interestingly, the high nucleation rate was also measured in the absence of water vapor for benzoic acid and *p*-toluic acid, indicating that binary nucleation of the organic acid–sulfuric acid system is responsible for the enhanced new particle formation. For benzoic and *p*-toluic acids and the experimental conditions similar to those in Figure 5.3, the measured particle concentrations were slightly higher (by about 10 to 20%) when the water flow in the aerosol chamber was turned off. Hence, these results suggest a probable interaction between the aromatic acid and sulfuric acid that leads to a reduced (heteromolecular) nucleation barrier.

We also examined (homomolecular) nucleation of the aromatic acids in the absence of sulfuric acid and water. New particle formation was only detected when a substantial saturation ratio was established in the aerosol chamber. The minimum S required to produce detectable new particles was about 45 for benzoic acid and even higher for *p*-toluic and *m*-toluic acids. Similarly, water was observed to have a negligible influence on the organic particle formation for benzoic and *p*-toluic acids, because the two organic acids are insoluble in water and the organic aerosols formed are

hydrophobic. In general, particle formation can be qualitatively predicted in terms of fundamental thermodynamic and kinetic principles [*Kathmann et al*., 2002]. The spontaneous gas-to-particle conversion process corresponds to a decreased free energy and is thermodynamically favorable but kinetically hindered. During nucleation, a thermodynamically stable cluster or critical embryo is generated before condensation growth of the particle, and this embryo formation involves an energy barrier. Also, condensation growth of nucleated critical embryos will be retarded because of increased activity due to the Kelvin barrier. Hence, particle nucleation and subsequent growth in a single-component system occur only if the system is supersaturated ($S > 1$). It is conceivable that large barriers generally exist for other carboxylic or dicarboxylic acids, as shown in our experiments for the aromatic acids. The atmospheric concentrations of the low-volatility organic compounds are typically at the ppb level or less, even under polluted conditions [*Finlayson-Pitts and Pitts*, 2000; *Seinfeld and Pandis*, 1998].

Although certain dicarboxylic acids do reach their saturation points in the atmosphere [*Chebbi and Carlier*, 1996], the high supersaturation required for homomolecular nucleation likely renders new particle formation from those compounds implausible. Previous smog chamber studies reported homogeneous nucleation from low-volatility organic compounds, but those experiments were carried out with the use of hydrocarbon concentrations that were several orders of magnitude higher than those found under the ambient conditions [*Hung et al.*, 1989;*Odum et al*., 1996].

5.3.3 Theoretical Calculation

To gain an insight into the nature of the interaction between aromatic and sulfuric acids at the molecular level, we performed quantum chemical calculations that show the formation of surprisingly stable aromatic acid–sulfuric acid complexes (see Figure 5.6). The equilibrium aromatic acid–sulfuric acid structure exhibits a nearly planar eight-membered ring: There are two hydrogen bonds, with the organic acid molecule acting as both a hydrogen bond donor and acceptor. The strength of the hydrogen bonding is reflected by the calculated bond lengths. For the benzoic–sulfuric acid complex, for example, the hydrogen bond is 1.503 Å for C=O···HOS and 1.705 Å for COH···O=S, nearly comparable to weak covalent bonds. The energetics of the complexes was quantified with a series of quantum chemical calculations as shown in Table 5.1. The bonding energies of the complexes are about 20 kcal mol^{-1} for benzoic and *p*-toluic acids and are about 4 kcal mol^{-1} higher for *m*-toluic acid. For comparison, the bonding energy is about 10 kcal mol^{-1} for the H_2O-H_2SO_4 complex [*Re et al*., 1999] and 25 kcal mol^{-1} for the H_2O-H_2SO_4-NH_3 system [*Larson et al*., 1999]. The large stability of the organic acid–sulfuric acid complex implies that the aromatic acid molecule bonds irreversibly to H_2SO_4 under atmospheric conditions. The complex formation between aromatic and sulfuric acids most likely reduces the barrier in heteromolecular nucleation and helps condensation growth of the nucleated critical embryo by overcoming the Kelvin effect, explaining the enhanced new particle formation observed in our experiments.

Additional calculations were performed for glutaric acid, indicating that stable complex formation with sulfuric acid represents a general feature for organic compounds with the carboxylic or dicarboxylic functional group. It is likely, though, that for smaller organic acids the effect on H_2SO_4 nucleation may be less important than that observed for the aromatic acids. The bonding energy of complexes represents one of the factors that determine particle nucleation. Other physicochemical parameters, such as the surface tension and equilibrium vapor pressures of the nucleated single or multicomponent system, also influence new particle formation. For example, our experimental results indicated a negligible effect of glutaric acid ($C_5H_8O_4$) on sulfuric acid nucleation, although the bonding energy of this organic acid with sulfuric acid is 19.2 kcal mol^{-1}, comparable to those of the aromatic acid-sulfuric acid complexes.

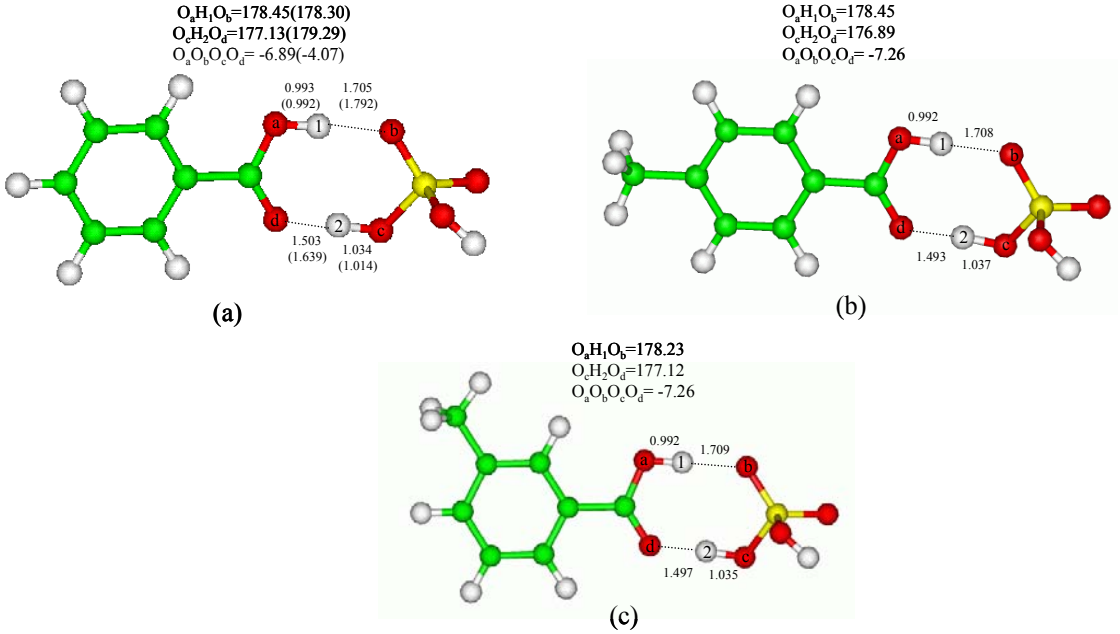

Figure 5.6. Equilibrium geometries of the benzoic acid (a), *p*-toluic acid (b), and *m*-toluic acid (c) - sulfuric acid complexes obtained at the B3LYP/6-31G(d,p) level of theory.

Table 5.1. Bonding energies, D_0 (in kcal mol^{-1}), of the aromatic acid—sulfuric acid complexes. BA-SA denotes benzoic acid— sulfuric acid complex; PTA-SA, *p*-toluic acid-sulfuric acid complex; and MTA-SA, *m*-toluic acid—sulfuric acid complex. All energies are corrected with the zero-point energies (ZPE).* The quantum chemical methods used in the present study are similar to those used by Suh *et al*. [2003]

Complex	D_0
BA-SA	19.85 [a]
	17.62 [b]
	18.63 [c]
	17.74 [d]
PTA-SA	19.99 [a]
MTA-SA	23.72 [a]

[a] Determined with B3LYP/6-31G(d,p)//B3LYP/6-31G(d,p)
[b] Determined with CCSD(T)/6-31G(d) + CF//B3LYP/6-31G(d,p)
[c] Determined with QCISD(T)/6-31G(d)//MP2(full)/6-31G(d).
[d] Determined with G2(MP2, SVP).
* provided by Zhao, J.

5.3.4 Atmospheric Implication

Organic acids have been widely identified as common components in atmospheric particulate matter [*Chebbi and Carlier*, 1996; *Kavouras et al*., 1998; *O'Down et al*., 2002; *Gasparini et al*., 2004]. Our experimental study shows that homomolecular nucleation of aromatic acids is unlikely to occur under atmospheric conditions, but that the interaction between aromatic acids and sulfuric acid promotes efficient heteromolecular nucleation. The gas-phase concentration of organic acids is substantially higher than that of gaseous H_2SO_4 in the atmosphere [*Chebbi et al*., 1996]; thus, organic acids can also contribute considerably to the initial growth of the newly nucleated embryos, which is important for subsequent particle growth by adsorption or heterogeneous reactions of other organic vapors. The particle formation mechanism proposed in this study can have major implications for SOA and sulfate aerosol formation in polluted areas, because both organic and sulfuric acids are photochemical degradation products linked to the emissions from the burning of fossil fuels [*Finlayson-Pitts and Pitts*, 2000; *Seinfeld and Pandis*, 1998]. In particular, new particle formation can occur efficiently over a large portion of northern America, eastern Asia, and some parts of central Europe because of the concurrent anthropogenic VOC and SO_2 emissions in those regions [*Tie et al*., 2003]. Our results suggest an alternative cause for efficient aerosol nucleation frequently observed in the polluted atmosphere, in addition to the available theories of water–sulfuric acid–ammonia ternary nucleation and ion-induced nucleation. For example, enhanced new particle formation (with a particle size of 3 to 4 nm) was observed in anthropogenic plumes advecting from Asia,

which were identified by elevated CO and SO_2 concentrations [*Weber et al.*, 2003]. The high CO amount was indicative of the abundance of VOCs inside those plumes. It was speculated that a high SO_2 concentration, in conjunction with other unidentified, possibly co-emitted species, was responsible for nucleation. In contrast, the same study revealed that few 3- to 4-nm particles were detected in the clean background and even within a volcanic plume that had a high H_2SO_4 but low CO concentration. Also, measurements of aerosol hygroscopicity during the 1999 Houston Supersite Project indicated a dominance of the organic matter in the fine particle mode, which could not be explained by the formation of ammonium sulfate [*Gasparini et al.*, 2004]. Those measurements likely can be explained by the importance of organic acids in particle nucleation and growth in the presence of sulfuric acid, because of the large abundance of both types of acids in urban environments and in the tropospheric boundary layer influenced by anthropogenic pollution.

5.4 Summary and Conclusions

The characteristics of several aromatic acids in the presence of the H_2O-H_2SO_4 binary system have been examined for their ability to promote the enhancement of new particle formation. Nanometer size distributions were obtained in order to obtain information on the nucleation mode, using nano-DMA and UFCPC operation system. The complex formation between aromatic and sulfuric acids most likely reduces the barrier in heteromolecular nucleation and helps condensation growth of the nucleated critical embryo by overcoming the Kelvin effect, explaining the enhanced new particle

formation observed in our experiments. Our results imply that the interaction between the organic acids-H_2O-H_2SO_4 system promotes the efficient aerosol nucleation frequently observed in the polluted atmosphere.

CHAPTER VI

SUMMARY AND CONCLUSIONS

This dissertation presents an oxidation mechanism of OH-toluene reactions and its relevance to organic aerosol formation. The theoretical results provide new insights into the mechanism of toluene oxidation in the atmosphere. The thermochemical and kinetic data allow for a quantitative assessment of the formation potential of ozone, dicarbonyls, and precursors of SOA. We determined the branching ratios of 0.52, 0.34, 0.11, 0.03 for the formation of *ortho*, *para*, *meta*, and *ipso* isomers, respectively, suggesting a strong preference for the *ortho* addition of OH to toluene. Our work confirms previous experimental and theoretical studies on the reversibility of the reaction fo the OH-toluene adduct with O_2. The results, however, suggest strong isomeric effects on the rate constants and equilibrium constants for this reaction. The relative stability and activation barriers of the peroxy radicals have negligible effect on isomeric branching of the OH-toluene reactions. Ozone production from the primary peroxy radicals is unimportant, since the peroxy radicals mainly cyclize to produce the bicyclic radicals rather than react with NO. Rearrangement of bicyclic radicals to more stable epoxides is too slow to matter because of the high activation barriers, and we conclude that there is negligible formation of epoxide carbonyls from the epoxide intermediates. At each OH attachment site, only one isomeric pathway via the bicyclic peroxy radical is accessible to lead to ring cleavage. The calculated decomposition rates for the acyclic radicals are in the range of $6x10^{-10}$ to $2x10^{14}$ s^{-1}. The results

suggest that fast decomposition rates of acyclic radicals provide significant glyoxal formation and dicarbonyl compounds such as 1,4- butenedial and 2-methyl-2-butenedial. These dicarbonyl compounds result in the formation of dihydro-2,5,-furandione, 2,5-furandione, and 3-methyl-2,5-furandione which have been seen as the primary SOA components.

The presented experimental results suggest the novel role of organic acids on new particle formation in the presence of the H_2O-H_2SO_4 binary system. The presence of the organic acids promotes new particle nucleation. Nanometer size distributions were obtained in order to obtain information on the nucleation mode. The surprisingly stable complex formation between aromatic and sulfuric acids explains the enhanced new particle formation observed in our experiments. Our results imply that the interaction between the organic acids-H_2O-H_2SO_4 system promotes the efficient aerosol nucleation frequently observed in the polluted atmosphere. The results provide an insight to understanding the events of large concentration of fine particle formation in the urban atmosphere, which strongly affects human health, radiation, and climate change.

If the interaction of H_2SO_4 with organic acids are included in aerosol models, the predicted SOA formation will be likely much greater and could have a much larger impact on climate forcing effects than presently predicted.

REFERENCES

Andino, J. M., J. N. Smith, R. C. Flagan, W. A. Goddard, and J. H. Seinfeld (1996), Mechanism of atmospheric photooxidation of aromatics: A theoretical study, *J. Phys. Chem.*, *100*, 10967-10980.

Atkinson, R. (1994), Gas-phase tropospheric chemistry of organic-compounds, *J. Phys. Chem. Ref. Data*. Monogr., 2.

Atkinson, R., S. M. Aschmann, J. Arey, and E. C. Tuazon (1994), Formation yields of epoxides and O(P(3)) atoms from the gas-phase reactions of O(3) with a serious of alkenes, *Int. J. Chem. Kinet*., *26*, 945-950.

Atkinson, R., D. L. Baulch, R. A. Cox, R. F. Hampson, J. A. Kerr, M. J. Rossi, and J. Troe (1997), Evaluated kinetic and photochemical data for atmospheric chemistry: Supplement VI - IUPAC subcommittee on gas kinetic data evaluation for atmospheric chemistry, *J. Phys. Chem. Ref. Data, 26*, 1329-1499.

Ball, S. M., D. R. Hanson, F. L. Eisele, and P. H. McMurry (1999), Laboratory studies of particle nucleation: Initial results for H2SO4, H2O, and NH3 vapors, *J. Geophys. Res., 104*, 23709-23718.

Bartolotti, L. J., and E. O. Edney (1995), Density-functional theory derived intermediates from the OH initiated atmospheric oxidation of toluene, *Chem. Phys. Lett*., *245*, 119-122.

Blando, J. D., and B. J. Turpin (2000), Secondary organic aerosol formation in cloud and fog droplets: A literature evaluation of plausibility, *Atmos. Environ*., *34*, 1623-1635.

Bohn, B. (2001), Formation of peroxy radicals from OH-toluene adducts and O_2, *J. Phys. Chem*., *105*, 6092-6101.

Bourmada, N., P. Devolder, and L. R. Sochet (1988), Rate-constant for the termolecular reaction of OH+toluene+helium in the fall-off range below 10 Torr, *Chem. Phys. Lett*., *149*, 339-342.

Boy, M., U. Rannik, K. E. J. Lehtinen, V. Tarvainen, H. Hakola, and M. Kulmala (2003), Nucleation events in the continental boundary layer: Long-term statistical analyses of aerosol relevant characteristics *J. Geophys. Res., 108*(D21), 4667, 0.1029/2003JD003838.

Calvert, J. G., R. Atkinson, K. H. Becker, R. M. Kamens, J. H. Seinfeld, T. J. Wallington, and G. Yarwood (2002), *The Mechanisms of Atmospheric Oxidation of Aromatic Hydrocarbons*, Oxford University Press, New York.

Charlson, R. J, J. E. Lovelock, M. O. Andreae, and S. G.Warren (1987), Oceanic phytoplankton, atmospheric sulfur, cloud albedo and climate, *Nature*, *326*, 655-661.

Chebbi, A., and P. Carlier (1996), Carboxylic acids in the troposphere, occurrence, sources, and sinks: A review *Atmos. Environ.*, *30*, 4233-4249.

Finlayson-Pitts, B. J., and J. N. Pitts Jr. (2000), *Chemistry of the Upper and Lower Atmosphere: Theory, Experiments,and Applications,* Academic Press, San Diego, CA.

Forstner, H. J. L., R. C. Flagan, and J. H. Seinfeld (1997), Molecular speciation of secondary organic aerosol from photooxidation of the higher alkenes: 1-octene and 1-decene, *Environ. Sci. Technol*., *31*,1953-1964.

Fortner, E. C., J. Zhao, and R. Y. Zhang (2004), Development of ion drift-chemical ionization mass spectrometry, *Anal. Chem*., *76*, 5436-5440.

Frisch, M. J., G. W Trucks, H. B. Schlegel, G. E. Scuseria, Robb, M. A. Cheeseman, J. R.Zakrzewski, V. G. Montgomery, J. A., Stratmann, R. E. Burant, J. C. Dapprich, S. Millam, J. M. Daniels, A. D. Kudin, K. N. Strain, M. C. Farkas, O. Tomasi, J. Barone, V. Cossi, M. Cammi, R. Mennucci, B. Pomelli, C. Adamo, C. Clifford, S. Ochterski, J. Petersson, G. A. Ayala, P. Y. Cui, Q. Morokuma, K. Malick, D. K. Rabuck, A. D. Raghavachari, K. Foresman, J. B. Cioslowski, J. Ortiz, J. V. Stefanov, B. B. Liu, G. Liashenko, A. Piskorz, P. Komaromi, I. Gomperts, R. Martin, R. L. Fox, D. J. Keith, T. Al-Laham, M. A. Peng, C. Y. Nanayakkara, A. Gonzalez, C. Challacombe, M. Gill, P. M. W. Johnson, B. G. Chen, W. Wong, M. W. Andres, J. L. Head-Gordon, M. Replogle, and E. S. Pople (1998), *Gaussian 98*, Revision D.3, Gaussian Inc., Pittsburgh, PA.

Garcia-Cruz, I., M. Castro, and A. Vivier-Bunge (2000), DFT and MP2 molecular orbital determination of OH-toluene-O-2 isomeric structures in the atmospheric oxidation of toluene, *J. Comput. Chem*., *21*, 716-730.

Gasparini, R., R. J. Li, and D. R. Collins (2004), Integration of size distributions and size-resolved hygroscopicity measured during the Houston Supersite for compositional categorization of the aerosol, *Atmos. Environ*., *38*, 3285-3303.

Ghigo, G., and G. Tonachini (1998), Benzene oxidation in the troposphere. Theoretical investigation on the possible competition of three postulated reaction channels, *J. Am. Chem. Soc*., *120*, 6753-6757.

Griffin, R. J., D. R. Cocker, R. C. Flagan, and J. H. Seinfeld (1999), Organic aerosol formation from the oxidation of biogenic hydrocarbons, *J. Geophys. Res.*, *104*, 3555-3567.

Hemminki, K. A. (1983), Nucleic-acid adducts of chemical carcinogens and mutagens, *Arch. Toxicol.*, *52*, 249-285.

Hoffmann, T., R. Bandur, U. Marggraf, and M. Linscheid (1998) Molecular composition of organic aerosols formed in the alpha-pinene/O-3 reaction: Implications for new particle formation processes, *J.Geophys. Res.*, *103*, 25569-25578.

Houghton, J. T. (Ed.) (2001), *Climate Change 2001: The Scientific Basis*, Cambridge Univ. Press, Cambridge.

Hung, C. H., M. Krasnopoler, and J. L. Katz (1989), Condensation of a supersaturated vapor .8. the homogeneous nucleation of n-nonane, *J. Chem. Phys.*, *90*, 1856-1865.

IPCC Scientific Assessment (1994), *Climate Change*, Cambridge University Press, Cambridge.

Jang, M. S., N. M. Czoschke, S. Lee, and R. M. Kamens (2002), Heterogeneous atmospheric aerosol production by acid-catalyzed particle-phase reactions, *Science*, *298*, 814-817.

Jang, M. S., and R. M. Kamens (2001), Characterization of secondary aerosol from the photooxidation of toluene in the presence of NOx and 1-propene, *Environ. Sci. Technol.*, *35*, 3626-3639.

Kathmann, S. M., G. K. Schenter, and B. C. Garrett (2002), Understanding the sensitivity of nucleation kinetics: A case study on water, *J. Chem. Phys.*, *116*, 5046-5057.

Kavouras, I. G., N. Mihalopoulos, and E. G. Stephanou (1998), Formation of atmospheric particles from organic acids produced by forests, *Nature*, *395*, 683-686.

Kleindienst, T. E., D. F. Smith, W. Li, E. O. Edney, D. J. Driscoll, R. E. Speer, and W. S. Weathers (1999), Secondary organic aerosol formation from the oxidation of aromatic hydrocarbons in the presence of dry submicron ammonium sulfate aerosol, *Atmos. Environ.*, *33*, 3669-3681.

Klotz, B., S. Sorensen, I. Barnes, K. H. Becker, T. Etzkorn, R. Volkamer, U. Platt, K. Wirtz, and M. Martin-Reviejo (1998), Atmospheric oxidation of toluene in a large-volume outdoor photoreactor: In situ determination of ring-retaining product yields, *J. Phys. Chem.*, *102*, 10289-10299.

Knispel, R., R. Koch, M. Siese, and C. Zetzsch (1990), Adduct formation of OH radicals with benzene, toluene, and phenol and consecutive reactions of the adducts with NOx and O_2, *Ber. Bunsen-Ges. Phys. Chem., 94,* 1375-1379.

Kolb, C. E. (2002), Iodine's air of importance, *Nature*, *417*, 597-598.

Kulmala, M. (2003), How particles nucleate and grow, *Science*, *302*, 1000-1001.

Kulmala, M., U. Pirjola, and J. M. Makela (2000), Stable sulphate clusters as a source of new atmospheric particles, *Nature*, *404*, 66-69.

Larson, L. J., A. Largent, and F. M. Tao (1999), Structure of the sulfuric acid-ammonia system and the effect of water molecules in the gas phase, *J. Phys. Chem.*, *103*, 6786-6792.

Laskin, A., D. J. Gaspar, W. H. Wang, S. W. Hunt, J. P. Cowin, S. D. Colson, and B. J. Finlayson-Pitts (2003), Reactions at interfaces as a source of sulfate formation in sea-salt particles, *Science*, *301*, 340-344.

Lay, T. H., J. W. Bozzelli, and J. H. Seinfeld (1996), Atmospheric photochemical oxidation of benzene: Benzene plus OH and the benzene-OH adduct (hydroxyl-2,4-cyclohexadienyl) plus O_2, *J. Phys. Chem.*, *100*, 6543-6554.

Leach, K. B., R. M. Kamens, M. R. Strommen, and M. Jang (1999), Partitioning of semivolatile organic compounds in the presence of a secondary organic aerosol in a controlled atmosphere, *J. Atmos. Chem.*, *33*, 241-264.

Lee, S. H., J. M. Reeves, J. C. Wilson, D. E. Hunton, A. A. Viggiano, T. M. Miller, J. O. Ballenthin, and L. R. Lait (2003), Particle formation by ion nucleation in the upper troposphere and lower stratosphere, *Science*, *301*, 1886-1889.

Lei, W. F., A. Derecskei-Kovacs, and R. Y. Zhang (2000), *Ab initio* study of OH addition reaction to isoprene, *J. Chem. Phys.*, *113*, 5354-5360.

Lei, W. F., and R. Y. Zhang (2000), Chlorine atom addition reaction to isoprene: A theoretical study, *J. Chem. Phys.*, *113*, 153-157.

Lei, W. F., and R. Y. Zhang (2001), Theoretical study of hydroxyisoprene alkoxy radicals and their decomposition pathways, *J. Phys. Chem.*, *105*, 3808-3815.

Lei, W. F., R. Y. Zhang, L. T. Molina, and M. J. Molina (2002), Theoretical study of chloroalkenylperoxy radicals, *J. Phys. Chem.*, *106*, 6415-6420.

Lonneman, W. A., R. L. Seila, and J. J. Bufaline (1978), Ambient air hydrocarbon concentrations in florida, *Environ. Sci. Tech*., *12*, 459-463.

Molina, M. J., R. Y. Zhang, K. Broekhuizen, W. Lei, R. Navarro, and L. T. Molina (1999), Experimental study of intermediates from OH-initiated reactions of toluene, *J. Am. Chem. Soc*., *212*, 10225-10226.

Motta, F., G. Ghigo, and G. Tonachini (2002), Oxidative degradation of benzene in the troposphere. Theoretical mechanistic study of the formation of unsaturated dialdehydes and dialdehyde epoxides, *J. Phys. Chem*., *106*, 4411-4422.

Nelson, P. F., S. M. Quigley, and M. Y. Smith (1983), Sources of atmospheric hydrocarbons in Sydney – a quantitative determination using a source reconciliation technique, *Atmos. Environ*., *17*, 439-449.

O'Dowd, C. D., P. Aalto, K. Hameri, M. Kulmala, and T. Hoffmann (2002), Aerosol formation - atmospheric particles from organic vapours, *Nature*, *416*, 497-498.

Odum, J. R., T. Hoffmann, F. Bowman, D. Collins, R. C. Flagan, and J. H. Seinfeld (1996), Gas/particle partitioning and secondary organic aerosol yields, *Environ. Sci. Technol.*, *30*, 2580-2585.

Odum, J. R., T. P. W. Jungkamp, R. J. Griffin, R. C. Flagan, and J. H. Seinfeld (1997), The atmospheric aerosol-forming potential of whole gasoline vapor, *Science*, *276*, 96-99.

Orville, R. E., G. Huffines, J. Nielsen-Gammon, R. Y. Zhang, B. Ely, S. Steiger, S. Phillips, S. Allen, and W. Read (2001), Enhancement of cloud-to-ground lightning over Houston, Texas, *Geophys. Res. Lett.*, *28*, 2597-2600.

Pandis, S.N., R. A. Harley, G. R. Cass, and J. H. Seinfeld (1992), Secondary organic aerosol formation and transport, *Atmos. Environ*., *26*, 2269-2282.

Pandis, S.N., A. S. Wexler, and J. H. Seinfeld (1995), Dynamics of tropospheric aerosols, *J. Phys. Chem*, *99*, 9646-9659.

Pankow, J. F. (1994a), An absorption model of gas-particle partitioning of organic compounds in the atmosphere, *Atmos. Environ.*, *28*, 185-188.

Pankow, J. F. (1994b), An absorption model of the gas aerosol partitioning involved in the formation of secondary organic aerosol, *Atmos. Environ.*, *28*, 189-193.

Perry, R. A., R. Atkinson, and J. N. Pitts (1977), Kinetics and mechanism of gas-phase reaction of OH radicals with methoybenzene and O-cresol over temperature range 299-435 K, *J. Phys. Chem*., *81*, 1607-1611.

Re, S., Y. Osamura, and K. Morokuma (1999), Coexistence of neutral and ion-pair clusters of hydrated sulfuric acid H2SO4(H2O)n (n=1-5) - A molecular orbital study, *J. Phys. Chem.*, *103*, 3535-3547.

Seinfeld, J. H., and S. N. Pandis (1998), *Atmospheric Chemistry and Physics: From Air Pollution to Climate Change*, John Wiley & Sons, New York.

Shepson, P. B., E. O. Edney, and E. W. Corse (1984), Ring fragmentation reactions on the photooxidations of toluene and ortho-xylene, *J. Phys. Chem*., *88*, 4122-4126.

Sigsby. J.E., S. Tejada, W. Ray, J. M. Lang, and J. W. Duncan (1987), Volatile organic-compound emissions from 46 in-use passenger cars, *Environ. Sci. Technol*., *21*, 466-475.

Smith, D. F., C. D. McIver, and T. E. Kleindienstn (1998), Primary product distribution from the reaction of hydroxyl radicals with toluene at ppb NOX mixing ratios, *J. Atmos. Chem*., *30*, 209-228.

Stein, S. E., B. S. Rabinovitch (1973), Accurate evaluation of internal energy level sums and densities including anharmonic oscillatiors and hindered rotors, *J. Chem. Phys*., *58*, 2438-2445.

Strey, R., P. E. Wagner, and Y. Viisanen (1994), The problem of measuring homogeneous nucleation rates and the molecular contents of nuclei – progress in the form of nucleation pulse measurements, *J. Phys. Chem*., *98*, 7748-7758.

Suh, I., R. Y. Zhang, L. T. Molina, and M. J. Molina (2003), Oxidation mechanism of aromatic peroxy and bicyclic radicals from OH-toluene reactions, *J. Am.Chem. Soc.*, *125*, 12655-12665.

Suh, I., D. Zhang, R. Y. Zhang, L. T. Molina, and M. J. Molina (2002), Theoretical study of OH addition reaction to toluene, *Chem. Phys. Lett*., *364*, 454-462.

Suh, I., W. F. Lei, and R. Y. Zhang (2001), Experimental and theoretical studies of isoprene reaction with NO3, *J. Phys. Chem.*, *105*, 6471-6478.

Tie, X. X., L. Emmons, L. Horowitz, G. Brasseur, B. Ridley, E. Atlas, C. Stround, P. Hess, A. Klonecki, S. Madronich, R. Talbot, and J. Dibb (2003), Effect of sulfate aerosol on tropospheric NOx and ozone budgets: Model simulations and TOPSE evidence, *J. Geophys. Res. 108*(D4), 10.1029/ 2003JD003659.

Tobias, H. J., D. E. Beving, P. J. Ziemann, H. Sakurai, Z. Miriam, P. H. McMurry, D. Zarling, R. Waytulonis, and D. B. Kittelson (2001), Chemical analysis of diesel engine nanoparticles using a nano-dma/thermal desorption particle beam mass spectrometer, *Environ. Sci. Technol.*, *35*, 2233-2243.

Tokmakov, I. V., and M. C. Lin (2002), Kinetics and mechanism of the OH+C6H6 reaction: A detailed analysis with first-principles calculations, *J. Phys. Chem.*, *106*, 11309-11326.

Volkamer, R., U. Platt, and K. Wirtz (2001), Primary and secondary glyoxal formation from aromatics: Experimental evidence for the bicycloalkyl-radical pathway from benzene, toluene, and p-xylene, *J. Phys. Chem.*, *105*, 7865-7874.

Uc, V. H., I. Garcia-Cruz, A. Grand, and A. Vivier-Bunge (2001), Theoretical prediction of EPR coupling constants for the determination of the selectivity in the OH addition to toluene, *J. Phys. Chem.*, *105*, 6226-6231.

Uc, V. H., I. Garcia-Cruz, A. Hernandez-Laguna, and A. Vivier-Bunge (2000), New channels in the reaction mechanism of the atmospheric oxidation of toluene, *J. Phys. Chem.*, *104*, 7847-7855.

Wang, S.C., S. E. Paulsen, D. Grosjean, R. C. Flagan, and J. H. Seinfeld (1992), Aerosol formation and growth in atmospheric organic NOx systems .1. outdoor smog chamber studies of C-7-hydrocarbons and C-8-hydrocarbons, *Atmos. Environ.*, *26*, 403-420.

Weber, R. J., S. Lee, G. Chen, B. Wang, V. Kapustin, K. Moore, A. D. Clarke, L. Mauldin, E. Kosciuch, C. Cantrell, F Eisele, D. C. Thornton, A. R. Bandy, G. W. Sachse, and H. E. Fuelberg (2003), New particle formation in anthropogenic plumes advecting from Asia observed during TRACE-P, *J. Geophys. Res*. *108*(D21), 10.1029/ 2002JD003112.

Weber, R. J., P. H. McMurry, R. L. Mauldin, D. J. Tanner, F. L. Eisele, A. D. Clarke, and V. N. Kapustin (1999), New particle formation in the remote troposphere: A comparison of observations at various sites, *Geophys. Res. Lett.*, *26*, 307-310.

Yu, J. Z., and H. E. Jeffries (1997), Atmospheric photooxidation of alkylbenzenes .2. Evidence of formation of epoxide intermediates, *Atmos. Environ.*, *31*, 2281-2287.

Yu, F. Q., and R. P. Turco (2001), From molecular clusters to nanoparticles: Role of ambient ionization in tropospheric aerosol formation, *J. Geophys. Res.*, *106*, 4797-4814.

Zhang, R. Y., I. Suh, W. Lei, A. D. Clinkenbeard, and S. W. North (2000), Kinetic studies of OH-initiated reactions of isoprene, *J. Geophys. Res.*, *105*, 24627-24635.

Zhang, R. Y., I. Suh, J. Zhao, D. Zhang, E. C. Fortner, X. X. Tie, L. T. Molina, and M. J. Molina (2004), Atmospheric new particle formation enhanced by organic acids, *Science*, *304*, 1487-1490.

Zhang, R. Y., X. X. Tie, and D. W. Bond (2003), Impacts of anthropogenic and natural NOx sources over the US on tropospheric chemistry, *Proc. Natl. Acad. Sci.U.S.A.*, *100*, 1505-1509.

Zhang, D., and R. Y. Zhang (2002a), Mechanism of OH formation from ozonolysis of isoprene: A quantum-chemical study, *J. Am. Chem. Soc*., *124*, 2692-2703.

Zhang, D., and R. Y. Zhang (2002b), Unimolecular decomposition of nitrooxyalkyl radicals from NO3-isoprene reaction, *J. Chem. Phys*., *116*, 9721-9728.

Zhang, D., R. Y. Zhang, and D. T. Allen (2003), C-C bond fission pathways of chloroalkenyl alkoxy radicals, *J. Chem. Phys*., *118*, 1794-1801.

Zhao, J., and R. Y. Zhang (2004), Proton transfer reaction rate constants between hydronium ion (H3O(+)) and volatile organic compounds, *Atmos. Environ*., *38*, 2177-2185.

Zhao, J., R. Y. Zhang, and S. W. North (2003), Oxidation mechanism of delta-hydroxyisoprene alkoxy radicals: hydrogen abstraction versus 1,5 H-shift, *Chem. Phys. Lett*., *369*, 204-213.

VITA

Inseon Suh was born in Pusan, Korea on Sept 27, 1973. She earned her Bachelor of Science degree in Chemistry from Seoul Women's University in Seoul, Korea in February 1996. She received her M.S. in Atmospheric Sciences from Texas A&M University in August 2000.

She may be reached via email at *isuh@tamu.edu* or U.S. mail c/o Department of Atmospheric Sciences, Texas A&M University, 77843-3150.